International Journal of Heat and Mass Transfer 103 (2016) 1261–1279

Contents lists available at ScienceDirect

International Journal of Heat and Mass Transfer

journal homepage: www.elsevier.com/locate/ijhmt

Effects of two-phase inlet quality, mass velocity, flow orientation, and heating perimeter on flow boiling in a rectangular channel: Part 1 – Two-phase flow and heat transfer results

Chirag R. Kharangate, Lucas E. O'Neill, Issam Mudawar *

Boiling and Two-Phase Flow Laboratory (BTPFL), School of Mechanical Engineering, Purdue University, 585 Purdue Mall, West Lafayette, IN 47907, USA

ARTICLE INFO

Article history:
Received 11 March 2016
Received in revised form 11 May 2016
Accepted 13 May 2016
Available online 23 June 2016

Keywords:
Flow boiling heat transfer coefficient
Two-phase pressure drop
Saturated boiling
Gravity effects
Orientation effects

ABSTRACT

Lack of understanding of flow boiling behavior in reduced gravity poses a major challenge to the development of future space vehicles utilizing two-phase thermal control systems (TCSs). A cost effective method to investigating the influence of reduced gravity on flow boiling is to perform ground experiments at different orientations relative to Earth gravity. This paper is the first part of a two-part study aimed at exploring flow boiling mechanisms of FC-72 in a rectangular channel heated along one wall or two opposite walls. Experiments are performed in vertical upflow, vertical downflow and horizontal flow, subject to large variations in mass velocity, inlet quality and wall heat flux. Detailed measurements are used to investigate the influences of orientation, and therefore gravity, on boiling curve, local and average heat transfer coefficients, and pressure drop, and their relationship with interfacial behavior is captured with high-speed video. For horizontal flow, the effects of gravity are reflected in appreciable stratification across the channel at low mass velocities, with gravity aiding vapor removal from, and liquid return to the bottom heated wall, while accumulating vapor along the top heated wall. For vertical upflow and vertical downflow, with both single-sided and double-sided heating, there is far better symmetry in vapor formation along the channel. The heat transfer coefficient shows significant variations among the different orientations and heating configurations at low mass velocities, but becomes insensitive to orientation above 800 kg/m^2 s, proving inertia around this mass velocity is effective at negating any gravity effects. For low mass velocities, pressure drops are fairly equal for vertical upflow and vertical downflow, but greater than for horizontal flows. However, fairly equal pressure drops are achieved at high mass velocities for all orientations. Overall, this study proves that gravity effects on two-phase pressure drop and two-phase heat transfer are dictated mostly by mass velocity and, to a lesser extent, by inlet quality.

1. Introduction

1.1. Two-phase thermal management of high-flux devices

Advances in many electronics technologies, especially during the past two decades, have resulted in unprecedented increases in device functionality. Accompanying these advances, however, have been alarming increases in the amounts of waste heat at the device, module and system levels. Those increases brought to the forefront of electronics system design the task of removing the heat while maintaining acceptable device temperatures. And applications facing this challenge span a broad range of industries, including high performance computer chips, computer data centers, hybrid vehicle power electronics, X-ray medical devices, commercial and military avionics, and both laser and microwave directed-energy defense electronics [1].

Poor thermophysical properties have already precluded air as viable coolant in most of these applications, and shifted focus to liquid coolants, using both single-phase and two-phase cooling technologies. And while designers of thermal management systems favor the former, because of their relative simplicity and lower cost, single-phase liquid cooling is no longer capable of coping with the sharp increases in heat dissipation. This explains the recent surge in number of published articles addressing the design and thermal performance of two-phase thermal management systems. These systems offer appreciable increases in heat transfer coefficients associated with heat acquisition from the device by

* Corresponding author. Tel.: +1 (765) 494 5705; fax: +1 (765) 494 0539.
E-mail address: mudawar@ecn.purdue.edu (I. Mudawar).
URL: https://engineering.purdue.edu/BTPFL (I. Mudawar).

http://dx.doi.org/10.1016/j.ijheatmasstransfer.2016.05.060
0017-9310/

Nomenclature

Bo	Bond number, $g_e(\rho_f - \rho_g)D_h^2/\sigma$
D_h	hydraulic diameter of flow channel
G	mass velocity
g_e	Earth gravity
H	height of flow channel's cross-section
h	heat transfer coefficient
H_a	heated wall *a*
H_b	heated wall *b*
L	length
L_d	development length of flow channel
L_e	exit length of flow channel
L_h	heated length of flow channel
p	pressure
p_{in}	pressure at inlet to heated portion of channel
Δp	pressure drop across heated portion of channel
q''_w	wall heat flux
Re_f	liquid Reynolds number, $G(1 - x_e)D_h/\mu_f$
T	temperature
T_{in}	temperature at channel inlet
T_{sat}	saturation temperature
$T_{sat,in}$	saturation temperature at inlet to heated portion of channel
$T_{w,avg}$	spatial average of wall temperatures
W	width of flow channel's cross-section
x_e	thermodynamic equilibrium quality
z	axial coordinate measured from inlet to heated portion of channel

Greek symbol

θ	flow orientation angle
μ	dynamic viscosity
ρ	density
σ	surface tension

Subscripts

avg	spatial average
f	liquid
g	vapor
in	inlet to heated portion of channel
m	wall identifier (*a* for heater H_a or *b* for heater H_b)
n	axial thermocouple location
sat	saturated
w	wall

boiling, and ultimate heat rejection by condensation. The remarkable enhancement in boiling heat transfer effectiveness is derived from their ability to utilize both sensible and latent heat of the coolant compared to only sensible heat for single-phase counterparts.

One of the attractive attributes of two-phase thermal management systems is their ability to operate in a number of boiling schemes, which can be categorized into pool boiling thermosyphon [2,3], falling film [4,5], channel flow boiling [6], micro-channel boiling [7,8], jet impingement [9,10], and spray [11–13], as well as hybrid schemes [14] combining two or more boiling schemes.

1.2. Two-phase flow and heat transfer in future space missions

With multiple long duration space missions planned for the future, each subjected to wide ranging gravity environments, design of thermal management systems for these missions poses significant challenges. Most urgent among those is the need to greatly reduce the size and weight of all components comprising a space vehicle, including those tasked with the thermal management.

The tasks of heat acquisition (from crew and avionics), heat transport, and heat rejection (via condenser/radiation) onboard a space vehicle are tackled by a Thermal Control System (TCS). A TCS that relies on phase change is ideally suited to meet the needs of reducing system size and weight, by capitalizing upon the orders of magnitude enhancement in heat transfer coefficients associated with flow boiling and condensation compared to single-phase liquid systems [15]. But two-phase systems are also encountered in other space applications, such as the Fission Power System (FPS) using the Rankine power cycle [15,16].

Despite the obvious merits of two-phase systems, limited understanding of the effects of microgravity is one of the biggest obstacles to their implementation. This limited understanding has spurred a series of research efforts in pursuit of mechanistic understanding and predictive tools for all aspects of two-phase flow and heat transfer in microgravity, including adiabatic flow [17–20], flow boiling [21–26], and flow condensation [27–31].

1.3. Saturated versus subcooled inlet conditions in flow boiling

Flow boiling in a heated channel can be implemented by supplying the coolant in either saturated state, as a liquid–vapor mixture, or subcooled liquid state, at a temperature below the saturation temperature corresponding to inlet pressure. For equal inlet pressure and mass velocity, saturated and subcooled boiling produce vastly different two-phase flow patterns along the channel, which also lead to drastic differences in pressure drop, local heat transfer coefficient, and critical heat flux (CHF).

Subcooled boiling is especially advantageous for situations involving high heat fluxes, where cooling capacity of the working fluid is ameliorated by using its sensible in addition to latent heat. With high inlet subcooling, especially in conjunction with high mass velocity, void fraction is reduced everywhere along the flow tube, which decreases the likelihood for vapor blanket formation, a key precursor for CHF.

Despite the obvious merits of subcooled boiling, the ability to supply coolant in subcooled state in a TCS is highly system related, and may not be possible everywhere in a closed two-phase loop. For example, the avionics in a space vehicle are cooled by a series of cooling modules called 'cold plates'. The working fluid is typically supplied in subcooled state, and gradually loses its enthalpy along the loop. Therefore, cold plates connected closest to the pump can take full advantage of the fluid's subcooling, while those downstream must contend with saturated inlet conditions. For this reason, design of cooling hardware for avionics requires rigorous understanding and predictive tools for both subcooled and saturated inlet conditions. With much of the available literature dedicated to subcooled inlet conditions, the present study will be focused entirely on saturated inlet conditions.

1.4. Effects of channel inclination on flow boiling

Gravity influences flow boiling through buoyancy, which is proportional to the product of gravity and density difference between liquid and vapor. Researchers have relied on different testing platforms to simulate reduced gravity in two-phase flow and heat transfer experiments. They include drop towers, drop shafts,

parabolic flight aircraft, sounding rockets, and the international Space Station (ISS) [31]. However, such tests can be cost prohibitive, and often preclude the ability to amass large databases corresponding to broad ranges of operating conditions.

The most cost effective method to investigating the influence of reduced gravity on flow boiling is to perform a series of experiments at different flow orientations relative to Earth gravity. Using a rectangular flow channel, each orientation produces a partial component of gravity perpendicular to the heated wall(s) of the channel. A key disadvantage of this method is its inability to completely isolate the effects of gravity perpendicular to, from those parallel to the heated wall.

The effects of gravity or body force on flow boiling are felt mostly at low mass velocities, which are associated with weak inertia. Here, flow orientation has a major influence on interfacial structure everywhere along the channel, including the heated wall. Orientations that enhance vapor removal from, and liquid return to the heated wall are especially effective at delaying CHF compared to orientation that accumulate vapor against the heated wall.

Zhang et al. [32,33] investigated flow boiling in a rectangular channel that was heated along one wall. Their tests were performed by supplying slightly subcooled FC-72 to the channel over a range of mean inlet liquid velocities from 0.1 to 1.5 m/s. The influence of flow orientation was examined by performing tests at different channel inclinations in 45° increments. The lowest inlet velocity produced the most profound variations in interfacial behavior, which were reflected in substantial variations in CHF for different orientations. For the horizontal orientation with the heated wall facing upwards ($\theta = 0°$), flow boiling resembled pool boiling, with the buoyancy aiding vapor removal from, and liquid return to the heated wall. On the other hand, the opposite orientation of horizontal flow with the heated wall facing downwards ($\theta = 180°$) caused buoyancy to accumulate vapor against the heated wall, which was reflected in very low CHF value. Overall, buoyancy had an enhancing influence on CHF for the combination of vertical or near vertical upflow and upward facing heated wall. The opposite trend was achieved for the combination of vertical or near vertical downflow and downward facing heated wall. Vertical downflow was especially problematic because of the opposite influences of the downward-facing liquid drag and upward-facing buoyancy causing the vapor to move either in the flow direction when liquid drag is greater, opposite to the flow direction when buoyancy is greater, or even stagnate along the channel when the two forces are equal. Zhang et al. showed that the influence of flow orientation, and therefore gravity, diminishes with increasing inlet velocity. In fact, fairly equal CHF values were achieved irrespective of orientation once the inlet velocity approached 1.5 m/s. This minimum velocity culminating in equal CHF values is an important design parameter since it provides the thermal engineer great flexibility in selecting cooling channel orientation.

Konishi et al. [34] later performed similar flow boiling experiments in a rectangular channel featuring one heated wall at different orientations but with saturated inlet conditions associated with a finite inlet void fraction. Despite some similarities in CHF trends with flow orientation and mass velocity, increased void faction in the channel for saturated inlet conditions had a profound influence on interfacial behavior everywhere along the channel. This influence was also reflected in the value of minimum velocity corresponding to CHF independent of flow orientation.

1.5. Objective of study

This study is a part of a NASA project whose ultimate goal is to develop the Flow Boiling and Condensation Experiment (FBCE) for the International Space Station (ISS). The flow boiling channel and ancillary instrumentation used in this study closely resemble those of the ISS FBCE. The present two-part study is focused on the flow boiling portion of the project, and involves performing tests at different flow orientations relative to Earth gravity to gain a broad fundamental understanding of the influences of body force and mass velocity on two-phase flow and heat transfer for saturated inlet conditions.

This study is a follow up to a series of studies that have been undertaken at the Purdue University Boiling and Two-Phase Flow Laboratory (PU-BTPFL) to address the interrelated influences of mass velocity and flow orientation for subcooled [32,33] and saturated inlet conditions [34–36]. But a key focus of this study is addressing the added complexities of single-sided versus double-sided heated wall configurations. These two configurations were recently examined only for horizontal flow [37,38], and showed profound differences in interfacial behavior between the opposite heated walls at low velocities. In the present study, the single-sided and double-sided heating configurations will be tested in horizontal flow, Fig. 1(a), vertical upflow, Fig. 1(b), and vertical downflow, Fig. 1(c). The flow schematics in these figures, which will be discussed later in this paper, reflect saturated inlet conditions that produce a large vapor core along the channel.

This study will provide the most comprehensive assessment to date of the effects of mass velocity, flow orientation, and both single-sided and double-sided heating for saturated inlet conditions. Presented is a mechanistic understanding of observed and measured trends, and detailed predictive models for flow structure, liquid and vapor area fractions and velocities, pressure drop, and CHF. This first part of the study will explore the experimental trends, including flow visualization of the interfacial behavior, boiling curves, local and average heat transfer characteristics, and pressure drop, while the second part [39] will be dedicated entirely to CHF mechanisms and predictions.

2. Experimental methods

2.1. Flow boiling module

A highly instrumented flow boiling module is designed for the present experiments. As shown in Fig. 2(a) and (b), this module consists of three transparent polycarbonate plastic (Lexan) plates sandwiched between two aluminum support plates. The transparent plates allow optical access to the boiling flow along two opposite sidewalls. The middle Lexan plate is milled to produce a 2.5-mm by 5-mm rectangular channel. Fig. 2(c) shows the channel consisting of an upstream developing length of L_d = 327.9 mm, a heated length of L_h = 114.6 mm, and an exit section of L_e = 60.9 mm. A honeycomb flow straightener is inserted in the inlet of the channel to break any large eddies. The upstream developing length is 100 times the hydraulic diameter of the channel, which is intended to ensure fully developed flow upstream of the heated length. Two copper slabs are inserted into rectangular grooves on either side of the middle Lexan plate, serving as heated walls along the two opposite 2.5-mm wide walls of the channel's heated section.

Fluid pressure is measured at five locations along the channel: the first in the inlet port, two in the developing region, one just upstream of the heated region, and one just downstream of the heated region. Fluid temperature measurements are made with type-E thermocouples inserted into the flow in the inlet and outlet ports.

2.2. Construction of heated walls

Fig. 2(d) shows the detailed construction of the heated walls. Each heated wall contains six of 188-Ω, 4.5-mm wide and

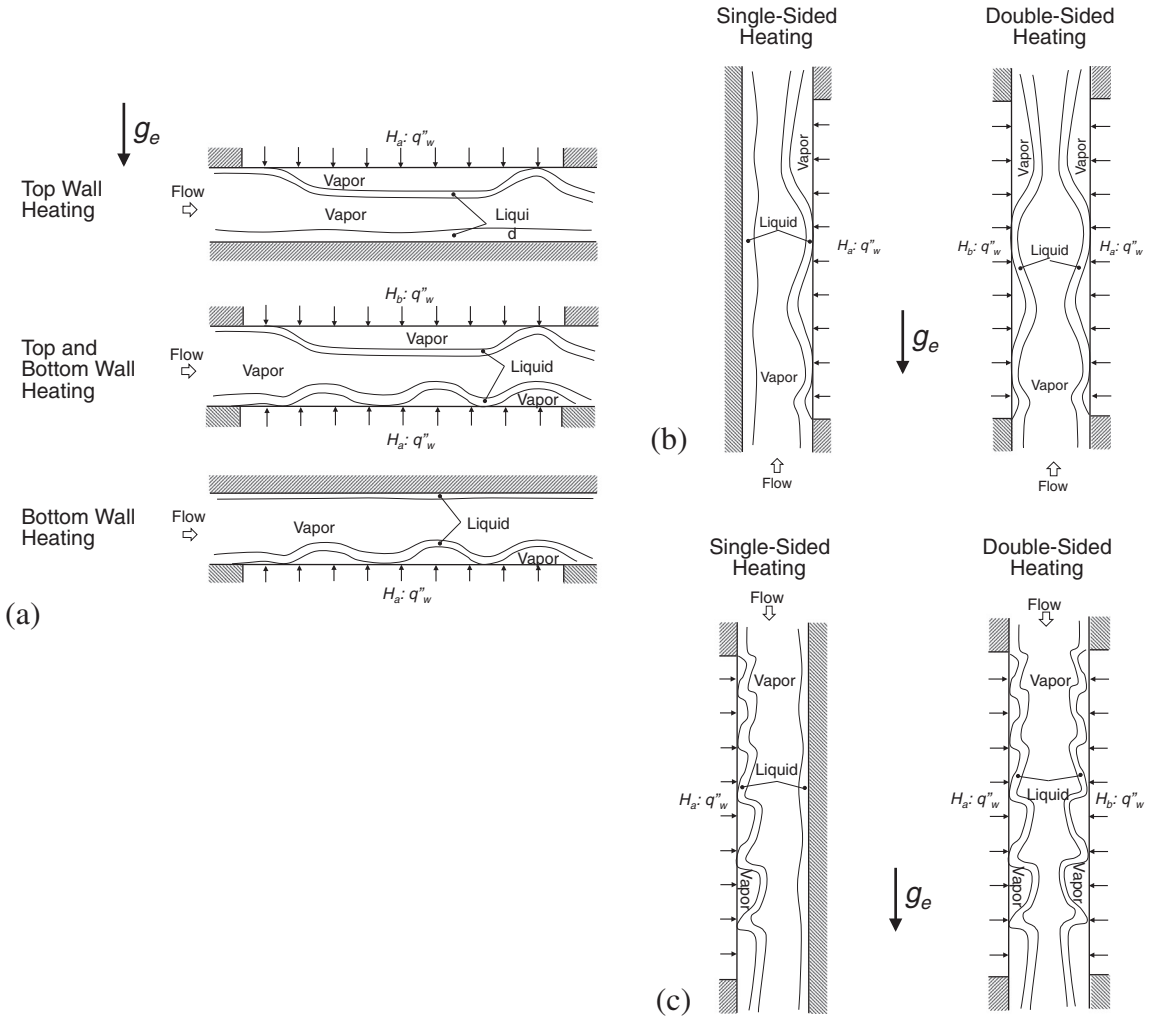

Fig. 1. Schematics for saturated flow boiling with single-sided and double-sided heating in (a) horizontal flow, (b) vertical upflow, and (c) vertical downflow orientations.

16.4-mm long thick-film resistors that are soldered to the backside of the copper slab. All resistors are connected in parallel to ensure uniform heat flux, and are powered by a single variable voltage source. Two sets of type-E thermocouples are inserted into shallow grooves between the resistors as shown in Fig. 2(e). One set is used for wall temperature measurements while the other is connected to a relay, set to automatically cut off power supply to the resistors should any of the wall temperatures exceed 130 °C, which indicates that CHF had already occurred. The thermocouples are designated as $T_{wm,n}$, where m represents the heated wall (H_a for heated wall a or H_b for heated wall b), and n the axial thermocouple location. The electrical control system allows power input to be turned on to one heated wall at a time, or to both walls simultaneously, in order to conduct either single-sided and double-sided heated wall experiments.

2.3. Fluid conditioning loop

The desired operating conditions at the inlet of the flow boiling module are achieved using the two-phase conditioning loop shown in Fig. 3(a). The working fluid, FC-72, is circulated in the loop using a magnetically coupled gear pump situated beneath the loop's reservoir. Exiting the pump, FC-72 liquid is passed through a filter, followed by a turbine flow meter before entering a set of two preheaters connected electrically in parallel to achieve a two-phase mixture at the inlet to the flow boiling module situated immediately downstream. The flow quality increases further due to heating along the flow boiling module. The two-phase mixture exiting the flow boiling module is passed through a water-cooled liquid-to-liquid heat exchanger, which converts the FC-72 back to liquid state before returning to the reservoir. The reservoir provides a reference pressure set point for the entire loop.

The flow boiling module, heater and temperature controls, and video camera system are mounted on a rigid optical table as shown in Fig. 3(b).

2.4. Flow visualization techniques

Two-phase interfacial features are captured along the heated portion of the flow channel with the aid of a high-speed camera. A fixed frame rate of 2000 frames per second (fps) and pixel resolution of 2040 × 156 are used to capture the entire heated length for each test run. Each video image sequence consists of 2000 frames, or 1.0-s of flow visualization data. Illumination is provided from the opposite side of the flow channel by four LEDs, with a light shaping diffuser (LSD) situated between the LEDs and the channel to enhance illumination uniformity.

2.5. Operating conditions, operating procedure, and measurement uncertainty

The operating conditions for the study are as follows: FC-72 inlet pressure of p_{in} = 109.7–191.8 kPa (15.9–27.8 psi), inlet temperature of T_{in} = 54.2–81.3 °C, mass velocity of

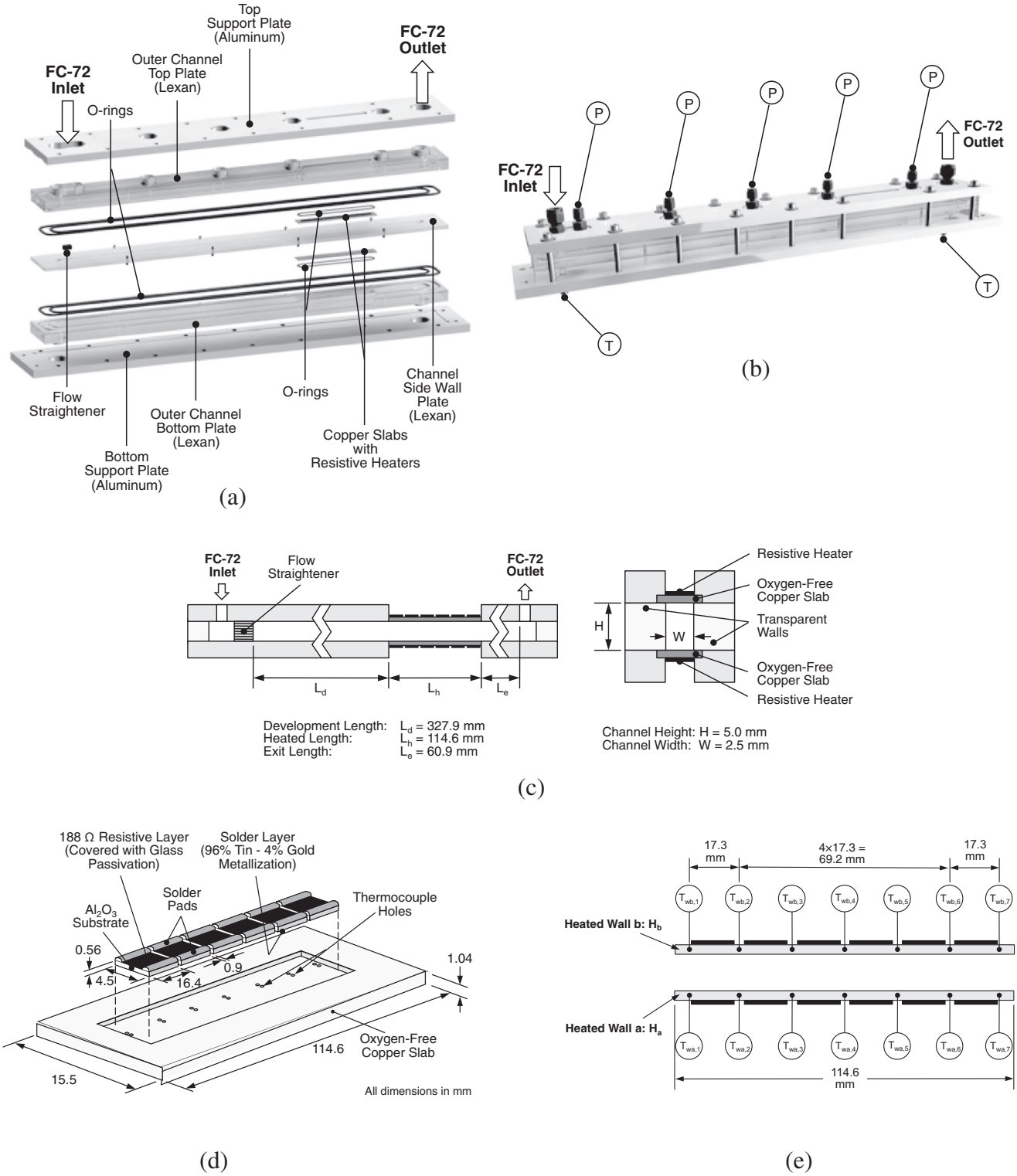

Fig. 2. (a) Exploded view of flow boiling module. (b) Assembled view of flow boiling module. (c) Key dimensions of flow channel. (d) Construction of heated walls and thick-film resistors. (e) Thermocouple layout in two heated walls.

G = 183.5–2030.3 kg/m^2 s, and inlet thermodynamic equilibrium quality of $x_{e,in}$ = 0.00–0.69. Li and Wu [40] developed a criterion for transition from conventional to micro/mini-channel flow behavior. Wu et al. [41] and Li and Wu [42] validated this criterion for CHF and pressure drop data, respectively. According to the criterion by Li and Wu [42], $BoRe_f^{0.5} > 200$ for all test cases of the present study. Therefore, macro-channel phenomena prevail for the entire study.

Once steady-state pressures, temperatures and flow rate are achieved everywhere in the loop, power is turned on to the specific heated wall or both walls, and a new waiting period is initiated before acquiring steady-state data and triggering the video camera

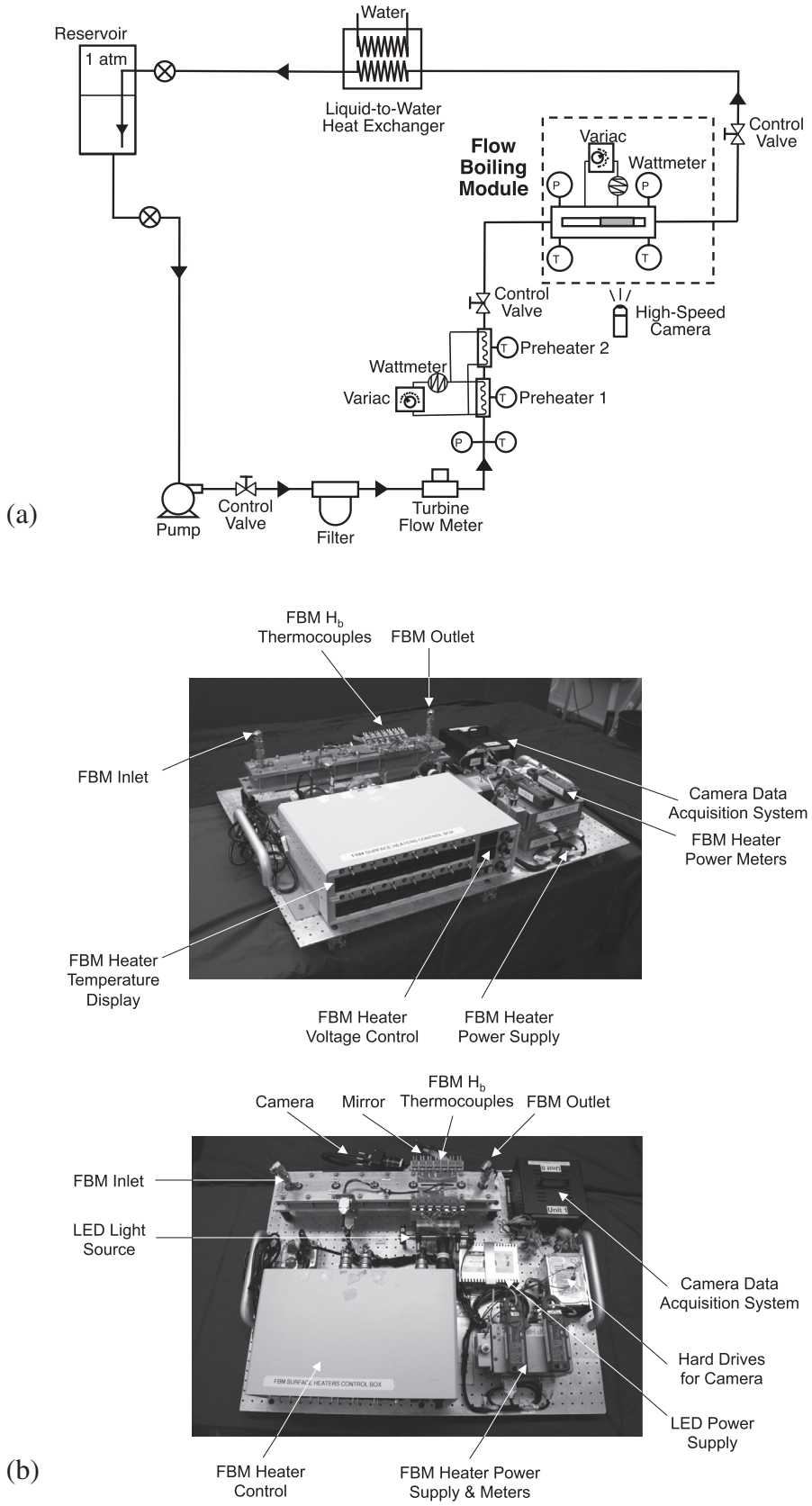

Fig. 3. (a) Flow loop diagram. (b) Photos of flow boiling module (FBM).

to record flow visualization data. The power is increased in several small increments and mass flow rate is maintained by adjusting the pump's rotational speed following each increment. The data are measured using a LabVIEW code in conjunction with an NI SCXI-1000 data acquisition system. To protect the heated walls against physical damage from CHF, the heated wall relays are

programmed to automatically cut off power supply to the heated walls should any of the wall temperatures exceed 130 °C.

Type-E thermocouples with an accuracy of ±0.5 °C are used to measure fluid and heated wall temperatures throughout the facility. Pressure measurements at the inlet of the upstream preheater and several locations along the flow boiling module are made with STS absolute pressure transducers with an accuracy of ±0.05%. The turbine flow meter has an accuracy of ±0.1%. The wall heat input is measured with an accuracy of ±0.5 W, and the overall uncertainty in determining the heat transfer coefficient is ±8%.

3. Flow visualization results

3.1. Flow orientation nomenclature

Fig. 4(a) and (b) illustrates the four flow orientations examined in this study for single-sided and double-sided heating, respectively. For all these orientations, the flow is shown entering from the center and radiating outwards. Three directions are tested: horizontal flow ($\theta = 0°$ and 180°), vertical upflow ($\theta = 90°$), and vertical downflow ($\theta = 270°$). For horizontal flow, two different orientations are tested for single-sided heating: upward-facing heated wall ($\theta = 0°$) and downward-facing heated wall ($\theta = 180°$). For horizontal flow with double-sided heating, the orientations $\theta = 0°$ and $\theta = 180°$ are identical due to symmetry, so only $\theta = 0°$ is tested.

Flow visualization at high mass velocities and high inlet qualities did not provide clear video images of the flow because high vapor shear at these conditions greatly reduced the thicknesses of the individual liquid and vapor layers adjacent to the heated wall, rendering identification of any near-wall effects quite elusive. Therefore, flow visualization results from only the low flow rate and low inlet quality tests are presented in this study.

3.2. Flow visualization results for horizontal flow

Using the schematics in Fig. 5(a) as guide, individual images of flow boiling along the entire heated portion of the channel are provided in Fig. 5(b)–(g) for horizontal flow with top wall heating, top and bottom wall heating, and bottom wall heating, and increasing heat flux (up to 91% CHF), at mass velocities of $G = 192.5–420.0$ kg/m^2 s with qualities at the inlet to the heated

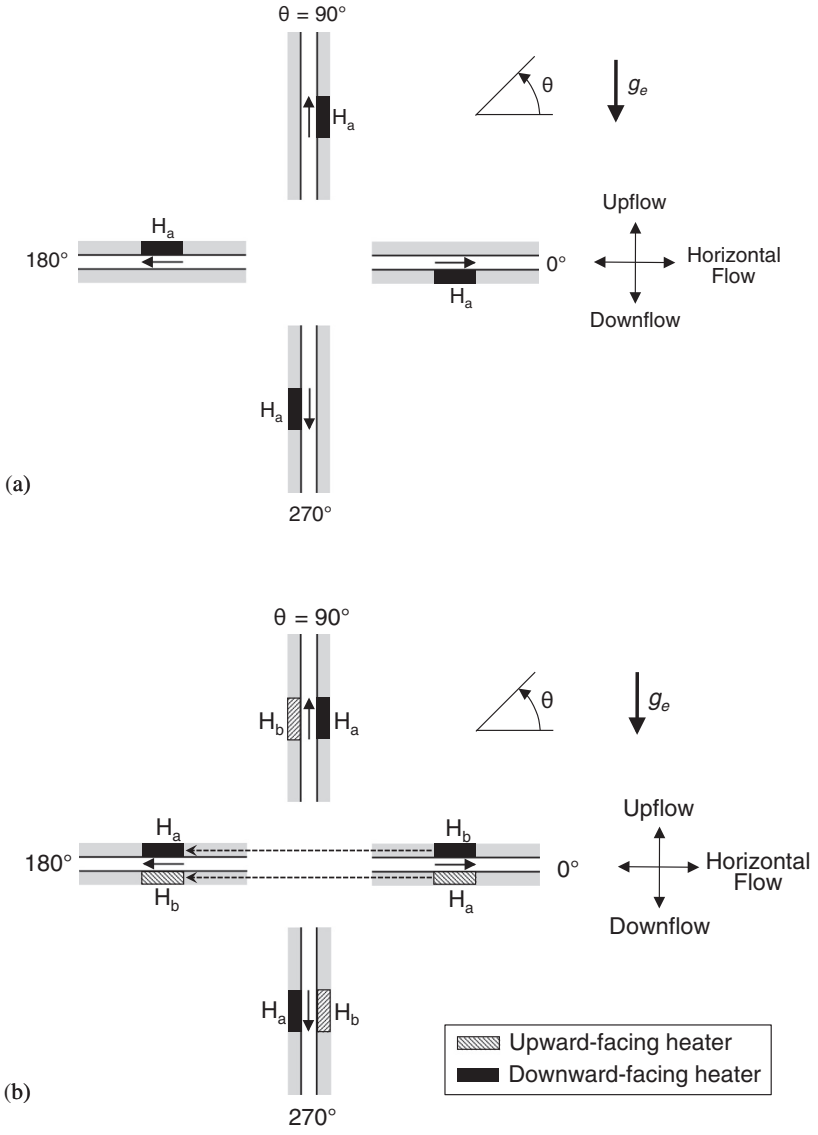

Fig. 4. Flow orientation and heater nomenclature for (a) single-sided heating and (b) double-sided heating in Earth gravity.

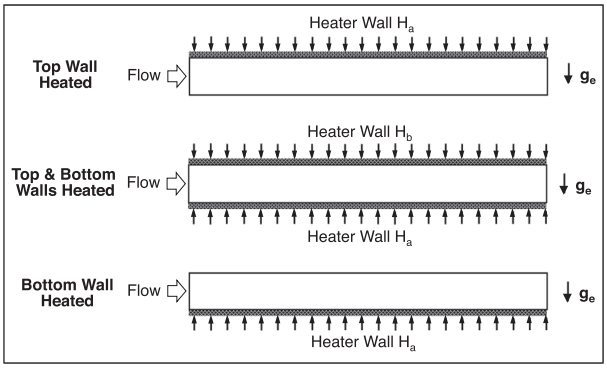

(a)

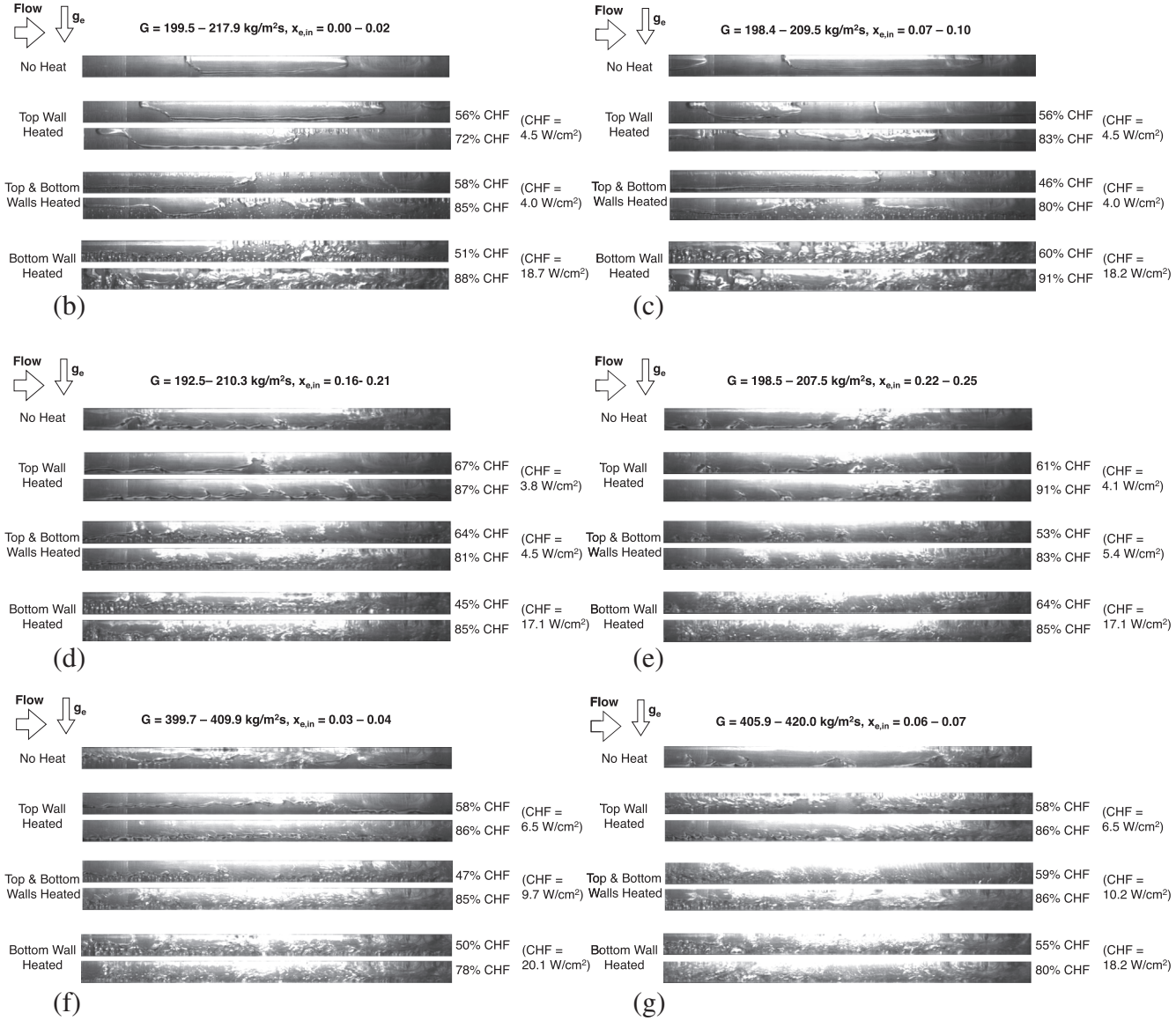

Fig. 5. (a) Heated wall configurations for horizontal flow, and corresponding variations of interfacial behavior with increasing heat flux for (b) G = 199.5–217.9 kg/m^2 s and $x_{e,in}$ = 0.00–0.02, (c) G = 198.4–209.5 kg/m^2 s and $x_{e,in}$ = 0.07–0.10, (d) G = 192.5–210.3 kg/m^2 s and $x_{e,in}$ = 0.16–0.21, (e) G = 198.5–207.5 kg/m^2 s and $x_{e,in}$ = 0.22–0.25, (f) G = 399.7–409.9 kg/m^2 s and $x_{e,in}$ = 0.03–0.04, and (g) G = 405.9–420.0 kg/m^2 s and $x_{e,in}$ = 0.06–0.07.

portion ranging from $x_{e,in}$ = 0.00 to 0.25. At G = 199.5–217.9 kg/m^2 s and $x_{e,in}$ = 0.00–0.02, Fig. 5(b), top wall heating shows vapor generated along the top wall combining with incoming elongated vapor bubbles, further increasing vapor accumulation along the heated wall. Top and bottom wall heating show similar behavior along the top wall, with small bubbles from the bottom wall migrating across the channel toward the top wall. For bottom wall heating, relatively large vapor bubbles generated along the bottom wall

are seen mixing with the incoming vapor, especially when the heat flux is increased. It is important to note that, for bottom wall heating, the heat flux values, including CHF, are substantially greater for bottom wall heating than the two other heating configurations. This behavior is caused by buoyancy aiding vapor removal from the bottom wall and wall replenishment with liquid, as described by Kharangate et al. [38] for a wide range of inlet conditions including $x_e > 0$. Similar interfacial behavior is observed for all three heated wall configurations for $x_{e,in} = 0.07–0.10$, Fig. 5(c). But as inlet quality is increased to $x_{e,in} = 0.16–0.21$ for fairly similar mass velocities, Fig. 5(d), the incoming vapor flow exhibits longer vapor bubbles and shorter liquid slugs. A further increase in inlet quality to $x_{e,in} = 0.22–0.25$, also at about the same mass velocity, Fig. 5(e), triggers liquid–vapor stratification along the entire channel, and heating along any or both walls causes the generated vapor to combine with the incoming stratified vapor. Fig. 5 (f) and (g) show images corresponding to higher mass velocity in the range of $G = 399.7–420.0$ kg/m^2 s. While the boiling behavior is not significantly different from that observed at the lower velocities in Fig. 5(b)–(e), there are signs of inertia sweeping interfacial features along the channel with greater intensity.

3.3. Flow visualization results for vertical upflow

The schematics in Fig. 6(a) serve as guide for the two heating configurations associated with vertical upflow. Fig. 6(b)–(e) shows individual images of flow boiling along the entire heated portion of the channel for vertical upflow with single-sided and double-sided heating for mass velocities in the range of $G = 210.6–236.3$ kg/m^2 s and two heat fluxes, with the inlet quality gradually increased from $x_e = 0.00–0.02$, Fig. 6(b), to $x_{e,in} = 0.17–0.19$, Fig. 6(e). Both single-sided and double-sided heating configurations show bubbles nucleating along the heated wall(s), with the increasing heat flux yielding larger coalescent vapor masses along the channel. The increase in inlet quality is shown culminating in elongated vapor bubbles entering the channel, which are shown growing and being distorted by the vapor generated along the heated wall(s). Fig. 6(f) shows similar interfacial behavior for the higher mass velocity of $G = 406.1–409.0$ kg/m^2 s. Overall, the main difference between vertical upflow and horizontal flow is a tendency for vapor in the former to flow symmetrically along the channel with no apparent bias towards either wall, while the vapor in horizontal flow has a clear tendency to stratify towards the top wall.

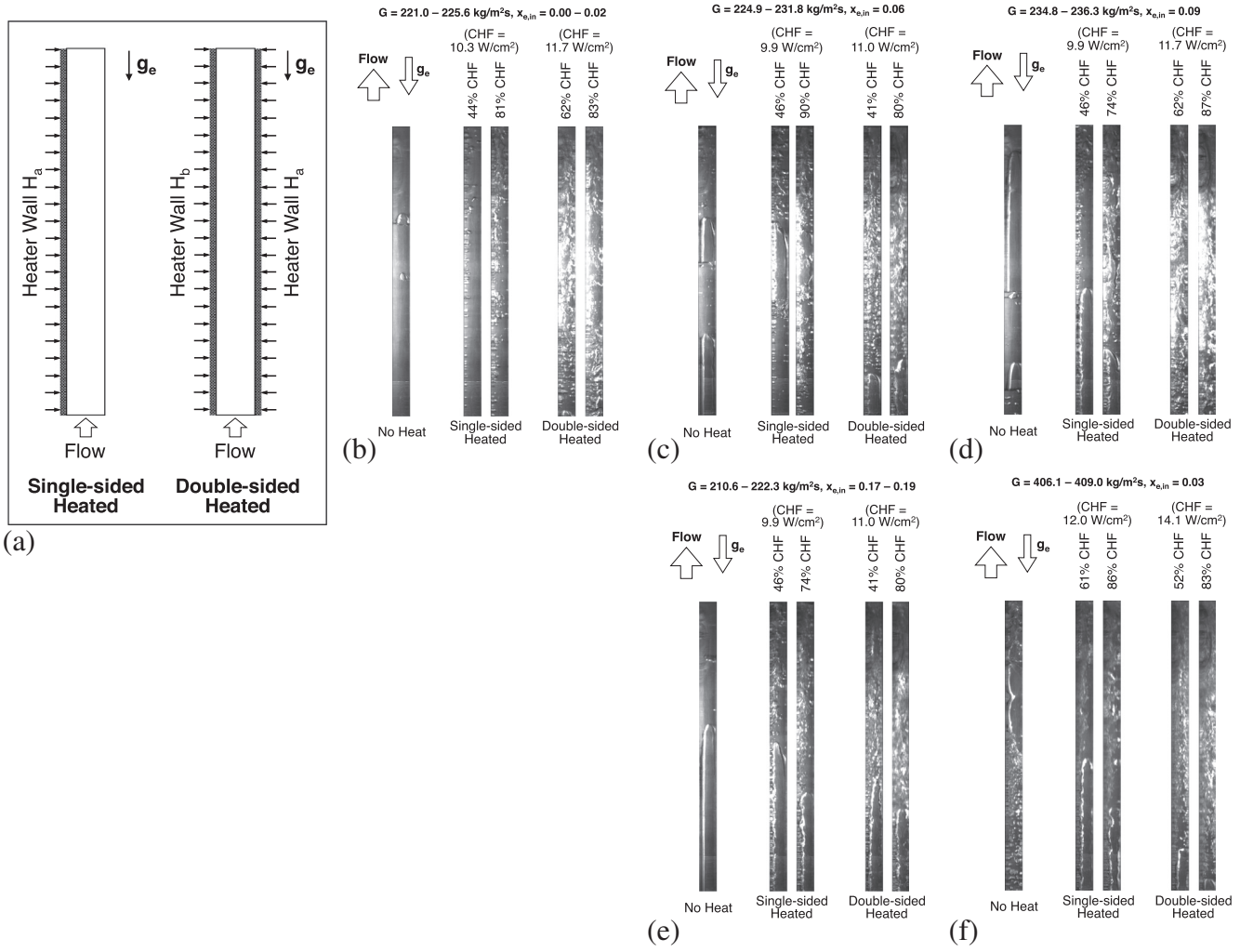

Fig. 6. (a) Heated wall configurations for vertical upflow, and corresponding variations of interfacial behavior with increasing heat flux for (b) $G = 221.0–225.6$ kg/m^2 s and $x_{e,in} = 0.00–0.02$, (c) $G = 224.9–231.8$ kg/m^2 s and $x_{e,in} = 0.06$, (d) $G = 234.8–236.3$ kg/m^2 s and $x_{e,in} = 0.09$, (e) $G = 210.6–222.3$ kg/m^2 s and $x_{e,in} = 0.17–0.19$, and (f) $G = 406.1–409.0$ kg/m^2 s and $x_{e,in} = 0.03$.

3.4. Flow visualization results for vertical downflow

Fig. 7(a) serves as guide for the two heating configurations used in conjunction with vertical downflow. Fig. 7(b) and (c) shows individual images of flow boiling along the entire heated portion of the channel for vertical downflow with single-sided and double-sided heating at mass velocities in the range of $G = 205.2–217.9$ kg/m^2 s and two heat fluxes, the main difference being a relatively low quality of $x_{e,in} = 0.01–0.03$ in Fig. 7(b), compared to a higher quality of $x_{e,in} = 0.09$ in Fig. 7(c). Both inlet quality ranges exhibit vapor coalescence in the heated portion of the channel into a large bubble. Fig. 7(d) and (e) shows images for a higher mass velocity range of $G = 405.4–422.0$ kg/m^2 s, with $x_e = 0.04–0.05$ and 0.07–0.08, respectively. With no heating, vapor is seen forming a large vapor bubble marred by many ripples along the vapor–liquid interface, which are caused by buoyancy acting opposite (upwards) to the main downflow direction. Increasing the heat flux for both heated wall configurations is reflected in increased vapor void along the heated portion of the channel.

4. Experimental results

4.1. Flow boiling curves

4.1.1. Flow boiling curves for horizontal flow

Fig. 8(a) shows flow boiling curves for horizontal flow with single-sided heating and different combinations of mass velocity and inlet quality. The boiling data are presented as variations of wall heat flux, q''_w, with the difference between average wall temperature, $T_{w,avg}$, and inlet saturation temperature, $T_{sat,in}$. The data exhibit typical flow boiling curve trends with the slope increasing appreciably around the region of initial bubble nucleation, and the wall temperature increasing sharply in an unsteady manner at CHF. Increasing the mass velocity is shown shifting the boiling curve to the left, indicating an enhancement in the heat transfer coefficient, as well as increasing CHF. Notice the large differences in heat transfer data for bottom wall heating compared to top wall heating, especially for the lowest mass velocities of $G = 198.4–206.2$ kg/m^2 s. The top wall heating is shown yielding

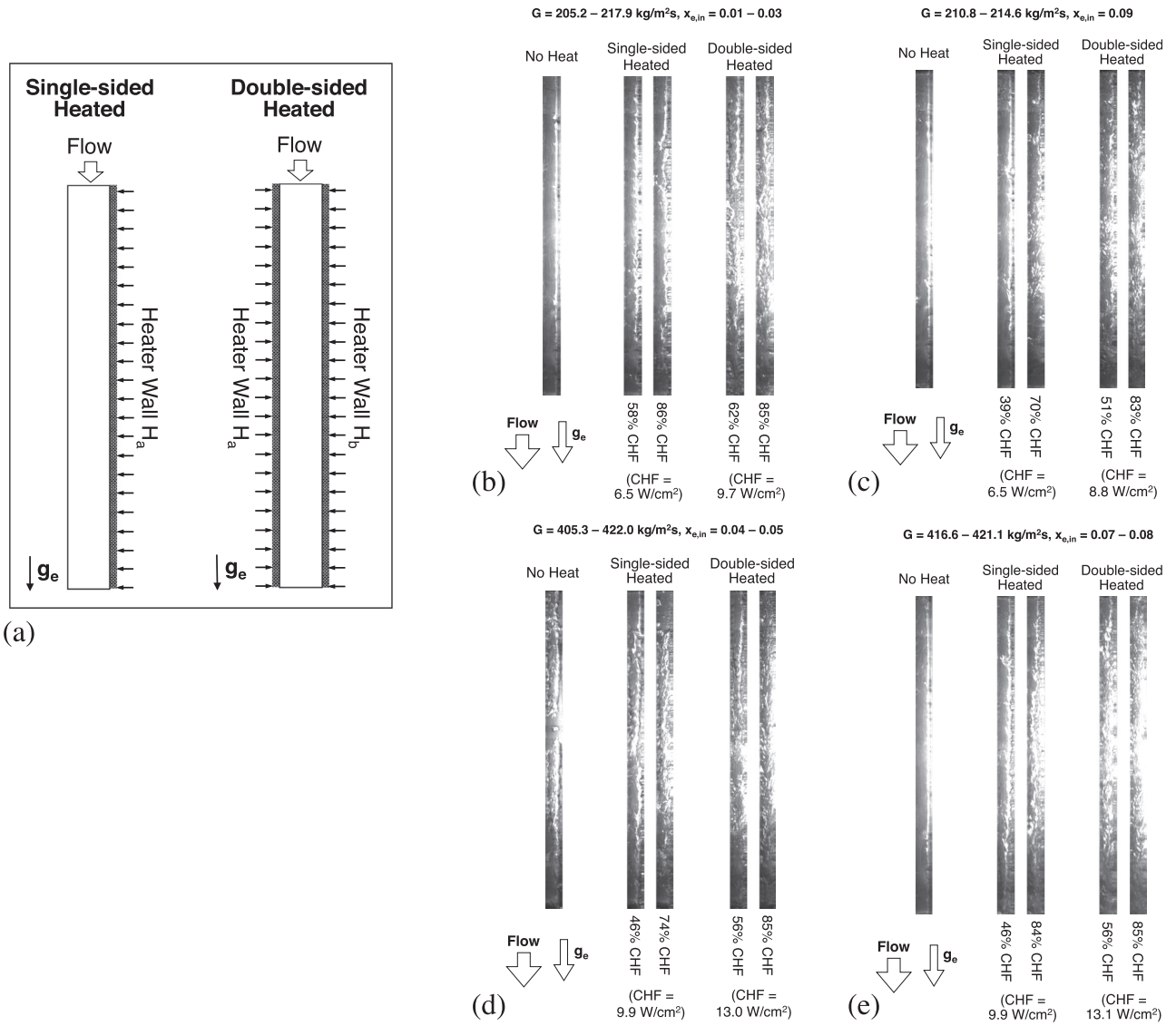

Fig. 7. (a) Heated wall configurations for vertical downflow, and corresponding variations of interfacial behavior with increasing heat flux for (b) $G = 205.2–217.9$ kg/m^2 s and $x_{e,in} = 0.01–0.03$, (c) $G = 210.8–214.6$ kg/m^2 s and $x_{e,in} = 0.09$, (d) $G = 405.3–422.0$ kg/m^2 s and $x_{e,in} = 0.04–0.05$, and (e) $G = 416.6–421.1$ kg/m^2 s and $x_{e,in} = 0.07–0.08$.

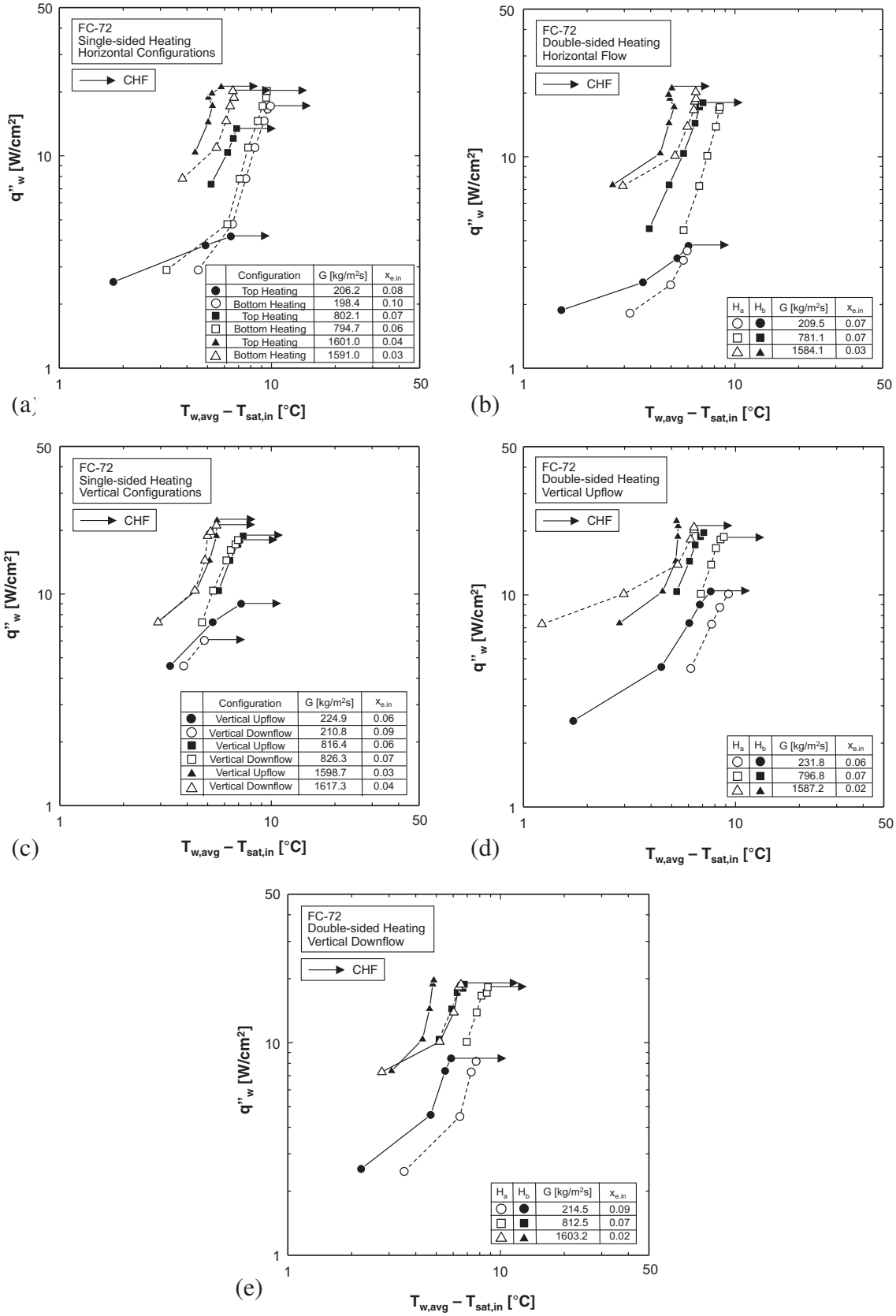

Fig. 8. Boiling curves for different inlet mass velocities for (a) single-sided heated horizontal flow, (b) double-sided heated horizontal flow, (c) single-sided heated vertical upflow and downflow, (d) double-sided heated vertical upflow, and (e) double-sided heated vertical downflow.

far more inferior heat transfer performance, which can be explained by the appreciable vapor stratification along the top wall as shown earlier in Fig. 5(c). Increasing the mass velocity in Fig. 8(a) is reflected by the top wall heating and bottom wall heating acquiring fairly equal slope, and the differences in heat transfer performance decreasing because of the increasing magnitude of flow inertia compared to buoyancy.

Fig. 8(b) shows flow boiling curves for horizontal flow with double-sided heating. While the top wall shows slightly higher heat transfer performance and triggers CHF consistently for all mass velocities, there is closer agreement in heat transfer data between the two heated walls for each mass velocity compared to those in Fig. 8(a). This trend can be explained by the two heated walls increasing void fraction, thereby increasing flow acceleration and better combating buoyancy effects compared to a single heated wall.

4.1.2. Flow boiling curves for vertical upflow

Fig. 8(c) shows flow boiling curves for both vertical upflow and vertical downflow with single-sided heating and different combinations of mass velocity and inlet quality. For vertical upflow, there is a monotonic enhancement in heat transfer performance and CHF with increasing mass velocity. A similar trend is observed in Fig. 8(d), which shows boiling curves for vertical upflow with double-sided heating. Because of symmetry, there is some randomness regarding which of the two walls provides the better performance in two-sided heating.

4.1.3. Flow boiling curves for vertical downflow

The boiling data for vertical downflow with single-sided heating is shown on Fig. 8(c), which reflects the same trends as those for vertical upflow with single-sided heating. This lack of differences between vertical upflow and vertical downflow is attributed to the saturated inlet conditions producing a central elongated vapor core that grows along the heated portion of the channel due to vapor production, while pushing liquid against both the heated and insulated walls, as observed in Fig. 6(c) for vertical upflow and Fig. 7(c) for vertical downflow. One major exception is a large difference in CHF for the lowest mass velocity, which can be explained by buoyancy playing a more significant role at low velocity compared to flow inertia. Fig. 8(e) shows general trends for double-sided vertical downflow resemble those for single-sided heating. Because of similarity in both the flow and heating boundaries, there is randomness as to which of the two walls provides the better performance.

4.2. Heat transfer coefficient

4.2.1. Average heat transfer coefficient

In this study, the FC-72 enters the channel as a saturated two-phase mixture at T_{sat}, and this temperature is maintained along the entire heated portion of the channel. The local heat transfer coefficient at each thermocouple location along the heated wall is defined as $h_{m,n} = q''_w/(T_{wm,n} - T_{sat})$, where q''_w is the wall heat flux, $T_{wm,n}$ the wall temperature measured along heated wall m ($m = a$ for H_a and b for H_b), and n the thermocouple location. The local heat transfer coefficient values are then spatially averaged to obtain h_{avg}.

Fig. 9(a) and (b) show variations of h_{avg} with wall heat flux for horizontal flow with single-sided heating and inlet qualities ranging from $x_{e,in} = 0.03$ to 0.63 for two ranges of mass velocity,

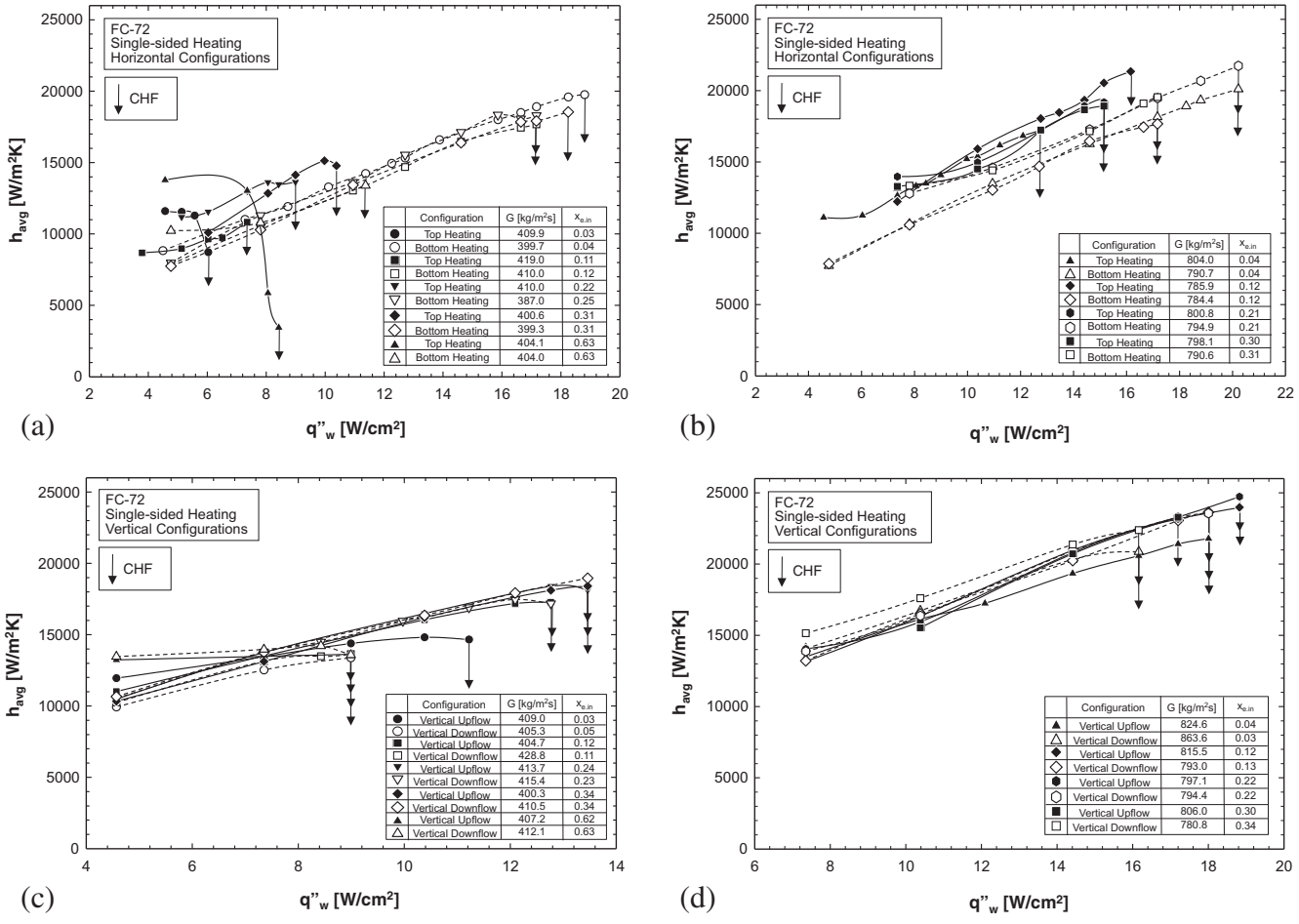

Fig. 9. Variations of average heat transfer coefficient with wall heat flux for single-sided heating with different inlet qualities for (a) horizontal configurations with $G = 387.0$–419.0 kg/m^2 s, (b) horizontal configurations with $G = 784.4$–804.0 kg/m^2 s, (c) vertical configurations with $G = 400.3$–428.8 kg/m^2 s, and (d) vertical configurations with $G = 780.8$–863.6 kg/m^2 s.

G = 387.0–419.0 kg/m^2 s and G = 784.4–804.0 kg/m^2 s, respectively. Overall, these figures show h_{avg} increasing monotonically with increasing wall heat flux. For the lower mass velocity range, Fig. 9(a) shows inlet quality having a measurable influence on h_{avg} for top wall heating, but a much weaker influence for bottom wall heating. The heat transfer performance for top wall heating at the highest inlet quality of $x_{e,in}$ = 0.63 is especially intriguing. Its behavior is drastically different in comparison with top wall heating with at an inlet quality of $x_{e,in}$ = 0.31. Two effects are encountered as inlet quality is increased from 0.31 to 0.63. They are (a) increased liquid and vapor velocity due to flow acceleration, and (b) increased vapor quality in the flow. The increase in quality causes a scarcity of liquid in the incoming flow, and therefore a very thin, high velocity liquid film is formed along the top wall, resulting in very high h_{avg} at low heat fluxes. But as the heat flux increases, partial dryout in the same liquid film drastically compromises h_{avg}, also paving the way for early CHF occurrence. Fig. 9(b) shows that increasing mass velocity provides better agreement between top wall and bottom wall heating, presumably because of increased flow inertia compared to buoyancy.

Fig. 9(c) and (d) shows h_{avg} results for vertical upflow and vertical downflow with single-sided heating with qualities in the range of $x_{e,in}$ = 0.03–0.63 and two ranges of mass velocity, G = 400.3–428.8 kg/m^2 s and G = 780.8–863.6 kg/m^2 s, respectively. For the lower mass velocity range, Fig. 9(c) shows far closer agreement in h_{avg} between vertical upflow and vertical downflow than horizontal flow, Fig. 9(a), proving these operating conditions correspond to flows dominated by inertia. With even stronger inertia for G = 780.8–863.6 kg/m^2 s, Fig. 9(d) shows even closer agreement between vertical upflow and vertical downflow.

Fig. 10(a) and (b) show variations of h_{avg} with wall heat flux for horizontal flow with double-sided heating and inlet qualities from $x_{e,in}$ = 0.03 to 0.63 for two ranges of mass velocity, G = 393.3–404.5 kg/m^2 s and G = 777.4–786.4 kg/m^2 s, respectively. Fig. 10(c) and (d) shows h_{avg} variations for vertical upflow with double-sided heating and inlet qualities from $x_{e,in}$ = 0.03 to 0.61 for G = 391.7–409.0 kg/m^2 s and G = 786.4–809.1 kg/m^2 s, respectively. Similarly, Fig. 10(e) and (f) shows h_{avg} plots for vertical downflow with double-sided heating and inlet qualities from $x_{e,in}$ = 0.03 to 0.61 for G = 394.9–427.3 kg/m^2 s and G = 782.1–844.7 kg/m^2 s, respectively. Overall, all these double-sided heating plots show heat transfer performance improving with increasing heat flux before suddenly declining at CHF. They also show the increase in mass velocity increasing the slope of h_{avg} versus wall heat flux. Fig. 10(a)–(f) also shows only minor differences in h_{avg} values between different orientations. Overall, these trends point to double-sided heating aiding vapor production and, therefore, flow acceleration, rendering inertia more effective at combating gravity effects. It is important to also note the differences in heat transfer performance between the two walls. Slight differences in electrical resistance between resistive heaters is responsible for small differences in heat flux input and therefore average heat transfer coefficients between the two walls. Physically, the two walls in vertical upflow and vertical downflow are symmetrical and, hence, should have equal heat transfer coefficients. In most cases, however, slight differences in electrical resistance between heated walls resulted in one wall outperforming the other in heat transfer performance. But in some cases, like Fig. 10(c) and (d), which correspond to higher qualities, the order of wall with the higher heat transfer performance is switched. This behavior is therefore the outcome of small experimental uncertainty and not related to any mechanistic behavior.

4.2.2. Local heat transfer coefficient results

Fig. 11(a)–(c) show variations of the local heat transfer coefficient, h, with distance, z, along the heated length for horizontal double-sided heating with G = 387.6–417.7 kg/m^2 s and different wall heat fluxes, with inlet qualities of $x_{e,in}$ = 0.06, 0.25, and 0.63, respectively. These figures show h increases monotonically with increasing heat flux at each thermocouple location. There is an appreciable decline in h in the inlet region, followed by a rather flat variation in the middle region, and a large increase in the exit region. The decrease in the inlet region is attributed to thermal boundary layer development, while the downstream increase is most likely the result of appreciable flow acceleration towards the exit. While it is difficult to quantify flow acceleration effects simply by examining the variations of local heat transfer coefficient, acceleration is expected in flow boiling configurations where the heat flux and/or inlet quality are increased. For each of the configurations examined in this study, local variations show that increasing the heat flux does shift the curve upwards, which can be attributed to flow acceleration. Additionally, by comparing Fig. 11(a)–(c), increasing inlet quality is shown to increase the heat transfer coefficient in the exit region, which is also attributed to flow acceleration. Overall, the three different inlet qualities show fairly similar performances.

4.2.3. Influence of orientation on heat transfer coefficient

A key objective of the present study is to assess the influence of gravity for different operating conditions. This is best achieved by comparing heat transfer results for the different flow orientations. Shown in Fig. 12(a)–(c) are polar plots for peak h_{avg} (obtained from Fig. 9(a)–(d)) for single-sided heating over a broad range of mass velocity, and inlet qualities of $x_{e,in}$ = 0.04–0.10, 0.14–0.22 and 0.30–0.36, respectively. For the lowest x_e range, Fig. 12(a) shows drastic differences in peak h_{avg} for horizontal bottom wall heating (θ = 0°) compared to top wall heating (θ = 180°) for the two lowest mass velocities. These differences are attributed to the stratification phenomenon discussed earlier, which tends to aid vapor removal from, and liquid return to the heated wall for θ = 0°, and compromise both for θ = 180°. These differences diminish with increasing mass velocity. Notice that peak h_{avg} values for vertical upflow (θ = 90°) and vertical downflow (θ = 270°) are about equal for the entire range of mass velocities, and values for all four orientations (θ = 0°, 90°, 180°, and 270°) are about equal above G = 794.7–826.3 kg/m^2 s, indicating inertia around this mass velocity range is effective at negating any gravity effects. Fairly similar trends can be seen in Fig. 12(b) and (c) corresponding to $x_{e,in}$ = 0.14–0.22 and 0.30–0.36, respectively. Therefore, for single-sided heating, the ability to negate gravity effects is determined mostly by mass velocity rather than inlet quality.

Fig. 13(a)–(c) show polar plots for peak h_{avg} for double-sided heating over a broad range of mass velocity, and inlet qualities of $x_{e,in}$ = 0.02–0.09, 0.13–0.19, and 0.30–0.36, respectively. A major fundamental feature of these plots is symmetry around the vertical axis. All three figures show fairly similar trends relative to mass velocity, with values for the lowest mass velocity range of G = 200.9–235.9 kg/m^2 s showing the greatest variations relative to orientation. Notice for these low mass velocities how vertical upflow (θ = 90°) and vertical downflow (θ = 270°) yield fairly equal peak h_{avg} values, which are significantly greater than those for horizontal flow (θ = 0° and 180°). The two horizontal orientations are quite unique in that they simultaneously combine heat transfer enhancement for the bottom heated wall and relatively poor heat transfer along the top heated wall. The polar trends in Fig. 13(a)–(c) for the lowest G range suggest bottom heated wall enhancement is too weak to compensate for the poor performance of the top heated wall. All three quality ranges show the influence of orientation on peak h_{avg} greatly diminishing with increasing G. Additionally, peak h_{avg} values begin to converge for all orientations at $x_{e,in}$ = 0.02–0.09, Fig. 13(a), and 0.13–0.19, Fig. 13(b), around the same range of G = 781.1–812.5 kg/m^2 s. However, the highest inlet

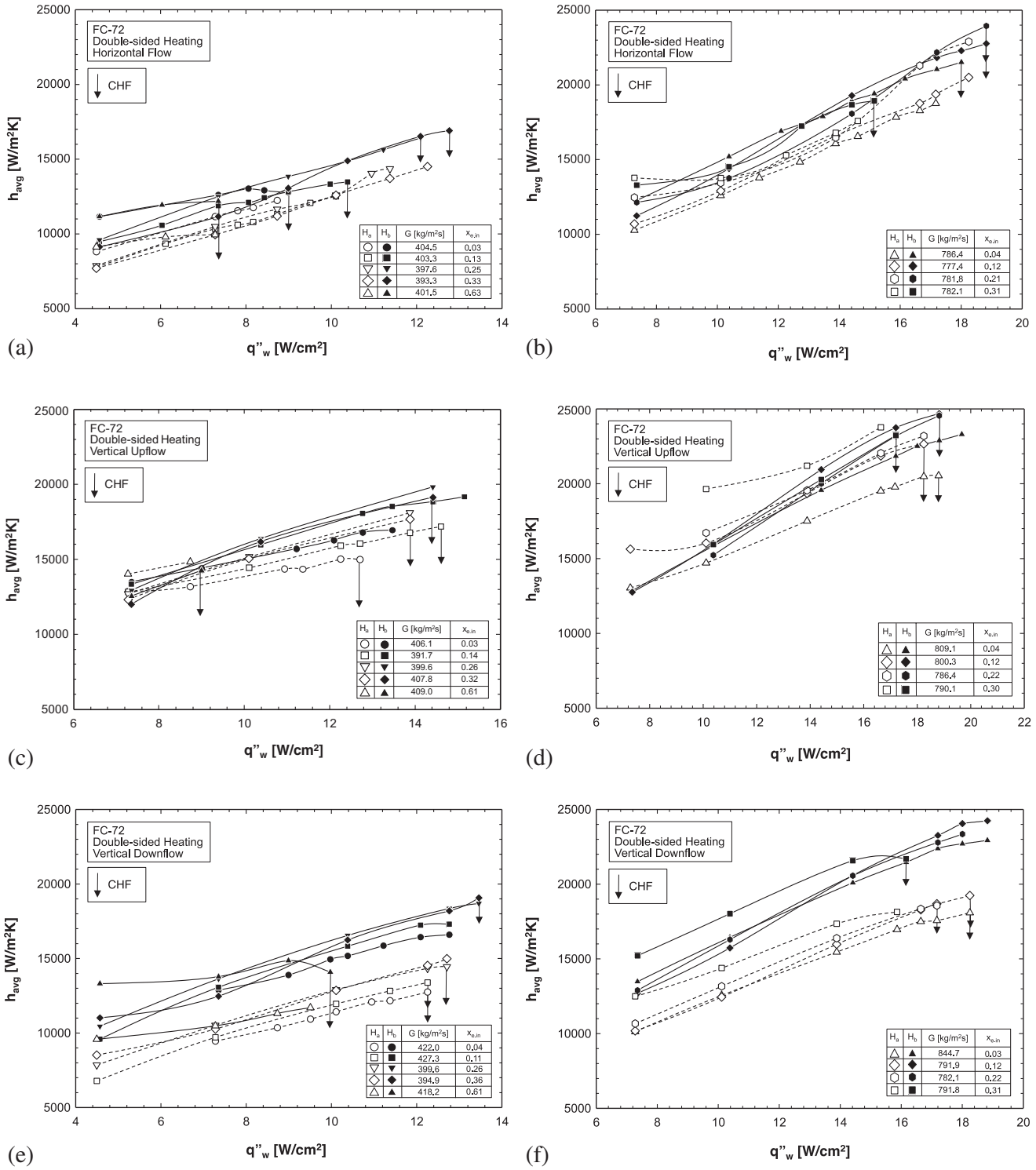

Fig. 10. Variations of average heat transfer coefficient with wall heat flux for double-sided heating with different inlet qualities for (a) horizontal flow with G = 393.3–404.5 kg/m^2 s, (b) horizontal flow with G = 777.4–786.4 kg/m^2 s, (c) vertical upflow with G = 391.7–409.0 kg/m^2 s, (d) vertical upflow with G = 786.4–809.1 kg/m^2 s, (e) vertical downflow with G = 394.9–427.3 kg/m^2 s, and (f) vertical downflow with G = 782.1–844.7 kg/m^2 s.

qualities of $x_{e,in}$ = 0.30–0.36, Fig. 13(c), reduce the influence of orientation for the lowest mass velocity range of G = 200.9–214.6 kg/m^2 s compared to the two lower quality ranges, presumably because of the higher flow acceleration provided by higher inlet quality. But equally interesting is how the highest inlet qualities of $x_{e,in}$ = 0.30–0.36 preserve a rather weak influence of orientation for other mass velocities. Overall, Fig. 13(a)–(c) prove that orientation effects are dictated mostly by mass velocity and, to a far lesser extent, by inlet quality.

4.3. Pressure drop

As indicated earlier, fluid pressure in the flow boiling module is measured at the module's inlet and outlet, as well as at several

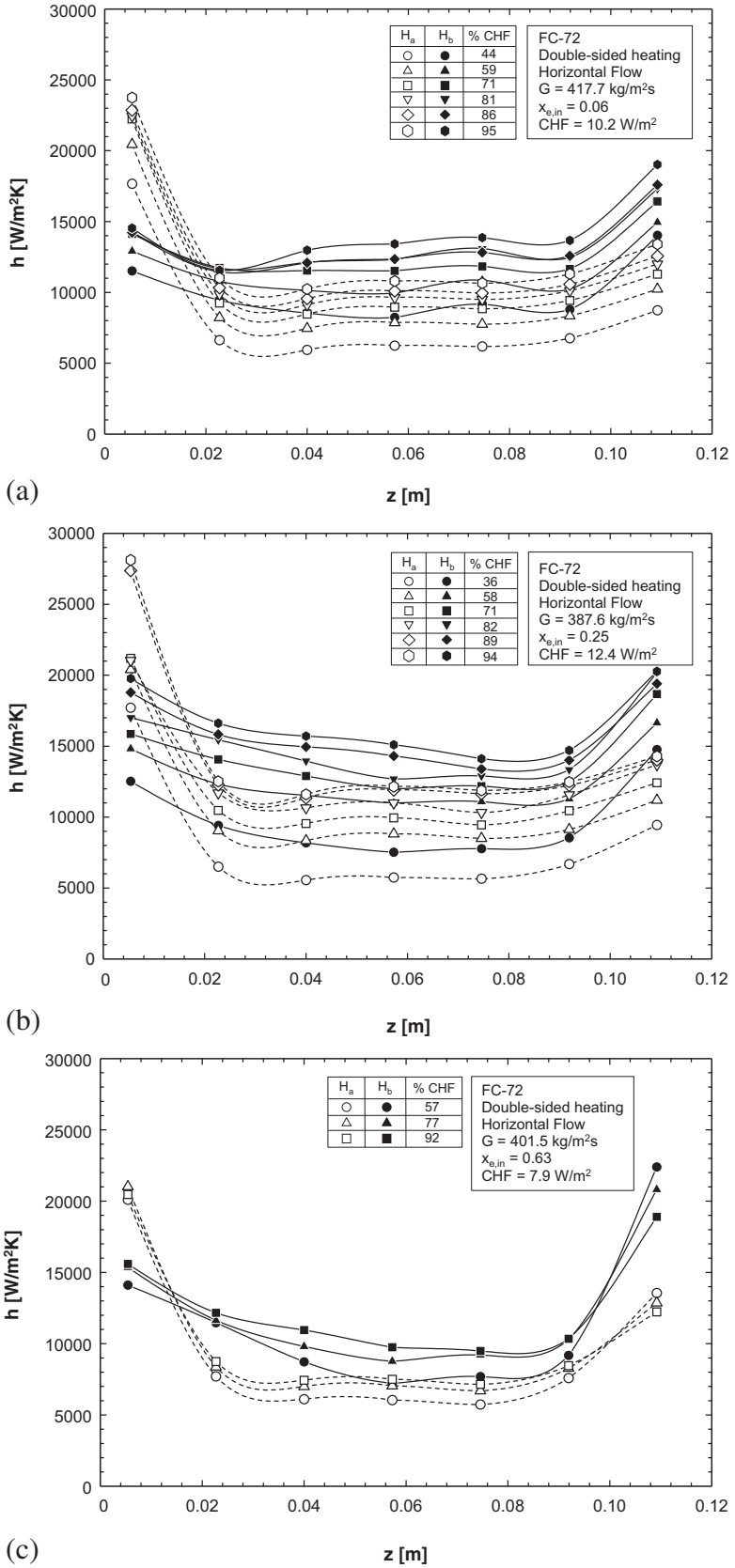

Fig. 11. Variations of local heat transfer coefficient along heated length of the channel for double-sided heating in horizontal orientation with increasing heat flux for G = 387.6–417.7 kg/m^2 s and (a) $x_{e,in}$ = 0.06, (b) $x_{e,in}$ = 0.25, and (c) $x_{e,in}$ = 0.63.

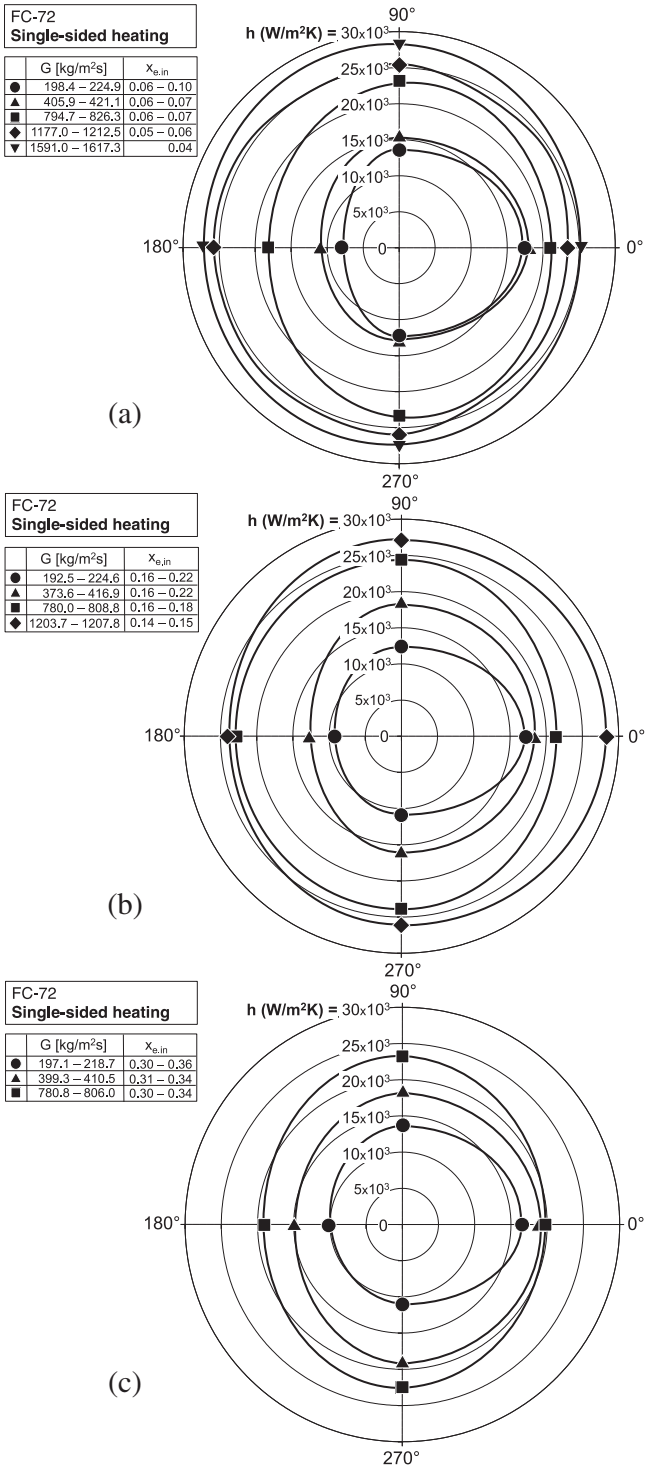

Fig. 12. Polar plots showing variations of peak heat transfer coefficient with orientation relative to Earth gravity for single-sided heating and different mass velocities, with (a) $x_{e,in}$ = 0.04–0.10, (b) $x_{e,in}$ = 0.14–0.22, and (c) $x_{e,in}$ = 0.30–0.36.

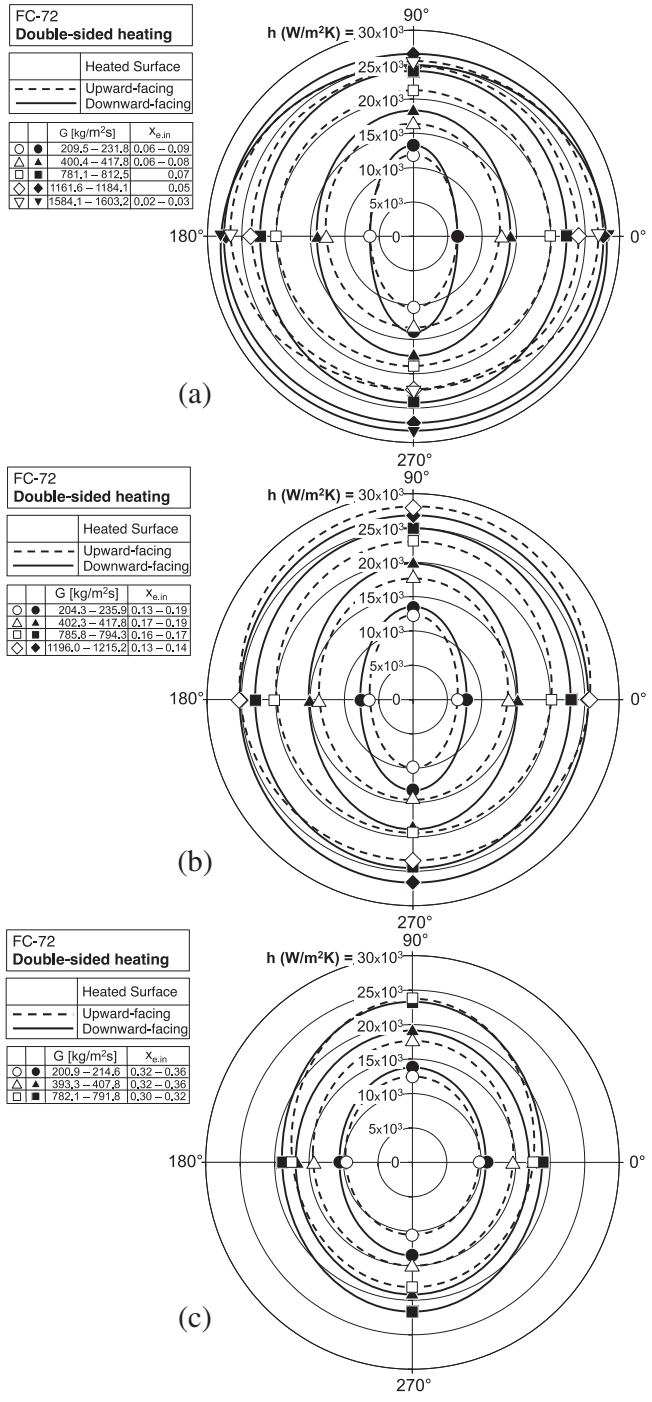

Fig. 13. Polar plots showing variations of peak heat transfer coefficient with orientation relative to Earth gravity for double-sided heating and different mass velocities for (a) $x_{e,in}$ = 0.02–0.09, (b) $x_{e,in}$ = 0.13–0.19, and (c) $x_{e,in}$ = 0.30–0.36.

locations along the flow channel. These include one pressure measurement just upstream, and another just downstream of the heated wall. Those two measurements are used to measure pressure drop, Δp, across the heated portion of the channel. To determine the influences of mass velocity, inlet quality, heating configuration, and orientation, the pressure drop values are compared for equal values of wall heat flux. Fig. 14(a)–(c) shows polar plots of Δp for single-sided heating configurations over a broad range of mass velocity and inlet qualities of $x_{e,in}$ = 0.04–0.07, 0.19–0.25, and 0.40–0.45, respectively. For the lowest quality range of $x_{e,in}$ = 0.06–0.07, Fig. 14(a) shows the lowest mass velocity ranges of G = 405.9–421.1 and 794.7–826.3 kg/m^2 s yielding higher Δp for vertical upflow (θ = 90°) and vertical downflow (θ = 270°) than the two horizontal flows (θ = 0° and 180°). Equally intriguing is that the two vertical flows show fairly equal Δp, even though the direction of gravity is reversed. Additionally, the two horizontal flows show equal Δp despite the opposite orientations of the heated walls. The fairly equal Δp values for vertical upflow and vertical downflow can be explained by the relative contributions of individual components of Δp. Two-phase pressure drop is

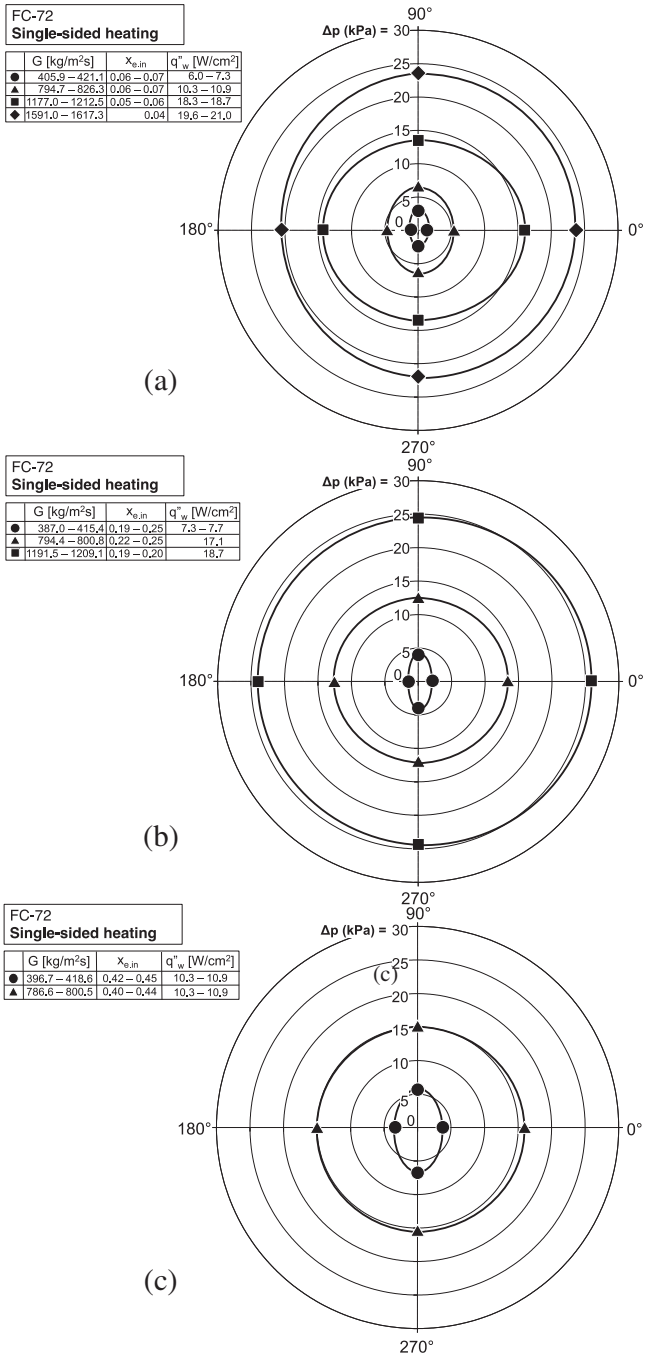

Fig. 14. Polar plots showing variations of pressure drop across heated portion of channel with orientation relative to Earth gravity for single-sided heating and different mass velocities for (a) $x_{e,in}$ = 0.04–0.07, (b) $x_{e,in}$ = 0.19–0.25, and (c) $x_{e,in}$ = 0.40–0.45.

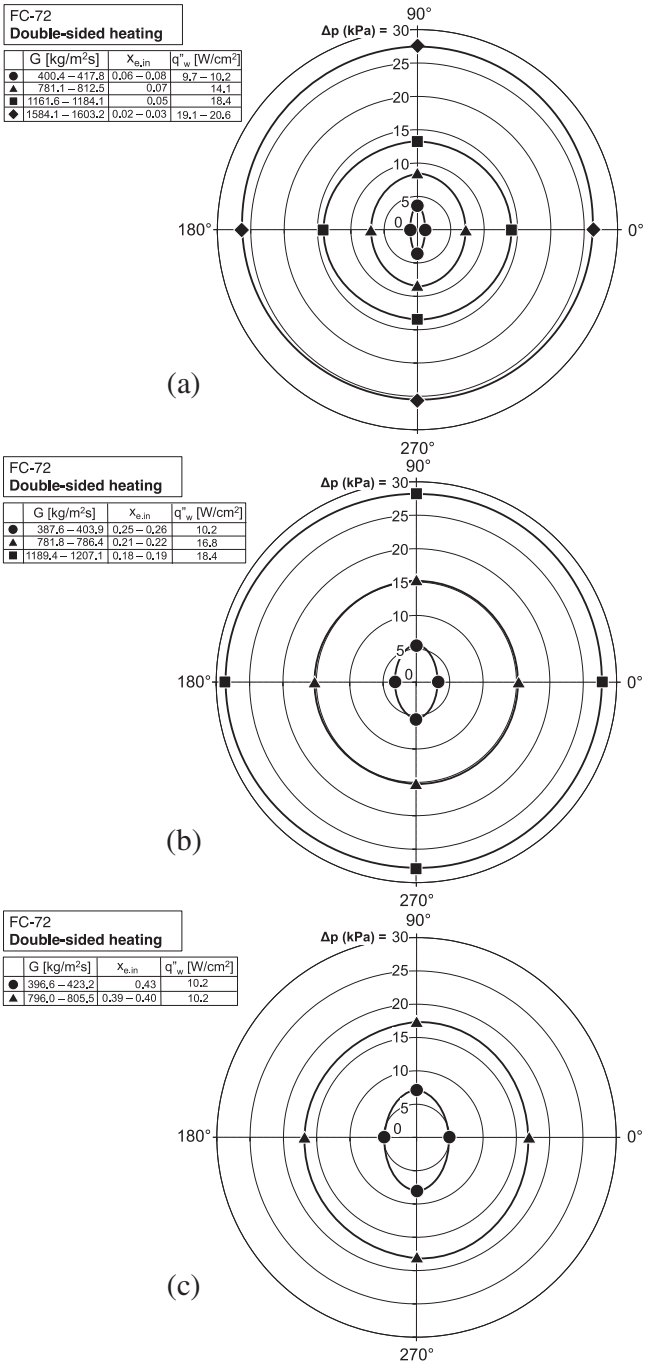

Fig. 15. Polar plots showing pressure drop across heated portion of channel with orientation relative to Earth gravity for double-sided heating and different mass velocities for (a) $x_{e,in}$ = 0.02–0.08, (b) $x_{e,in}$ = 0.18–0.26, and (c) $x_{e,in}$ = 0.39–0.43.

comprised of three components, friction, acceleration and gravitation, and the influence of orientation is reflected in the magnitude of the gravitational component, which is approximately proportional to the product of mean two-phase mixture density, Earth gravity, and length of heated portion of the channel. Given the large void fraction associated with these two orientations as discussed earlier in conjunction with the flow visualization results, the two-phase mixture density is quite small, rendering the contribution of the entire gravitational component negligible. The larger values for Δp for vertical upflow and vertical downflow compared to the two horizontal orientations can be explained by higher accelerational pressure drop for the vertical orientations. Notice how the influence of orientation on Δp decreases with increasing G. For the two higher inlet quality ranges of $x_{e,in}$ = 0.19–0.25 and 0.40–0.45, Fig. 14(b) and (c), respectively, show Δp values converge for all orientations around G = 786.6–800.8 kg/m^2 s, compared to a higher mass velocity of G = 1177.0–1212.5 kg/m^2 s for the lowest quality range of $x_{e,in}$ = 0.04–0.07 as shown in Fig. 14(a). Overall, Fig. 14(a)–(c) prove that orientation effects are dictated mostly by mass velocity and, to a lesser extent, by inlet quality.

Fig. 15(a)–(c) shows polar plots for Δp for double-sided heating over a broad range of mass velocity at inlet qualities of $x_{e,in}$ = 0.02–0.08, 0.18–0.26, and 0.39–0.43, respectively. A fundamental feature of these plots is symmetry around the

vertical axis. For the lowest quality range, Fig. 15(a) shows that Δp values at $G = 400.4–417.8$ kg/m^2 s for vertical upflow ($\theta = 90°$) and vertical downflow ($\theta = 270°$) are greater than for the two horizontal orientations, and the influence of orientation diminishes with increasing G. While this trend is similar to that for single-sided heating, Fig. 14(a), two-sided heating decreases the influence of orientation for $G = 781.1–812.5$ kg/m^2 s. The polar plots for the double-sided heating at $x_{e,in} = 0.18–0.26$, Fig. 15(b), and $x_{e,in} = 0.39–0.43$, Fig. 15(c), exhibit similar trends, with the influence of orientation becoming quite small starting around $G = 781.8–805.5$ kg/m^2 s. Once again, these trends prove that orientation effects are dictated mostly by mass velocity rather than inlet quality.

Comparing the Δp results for double-sided heating, Fig. 15(a)–(c), to those for single-sided heating, Fig. 14(a)–(c), reveals that, for identical values of G, $x_{e,in}$ and wall heat flux, Δp is generally higher for two-sided heating. This trend can be explained by the nearly twice the amount of vapor produced with double-sided heating.

5. Conclusions

This first part of a two-part study explored flow boiling of FC-72 along a rectangular channel with one wall or two opposite walls heated. Experiments were performed in three channel orientations: horizontal, vertical upflow, and vertical downflow over broad ranges of mass velocity, inlet quality and wall heat flux, aided by high-speed video capture of interfacial features. This first part was focused on the influence of gravity, and therefore orientation, on interfacial behavior during flow boiling, boiling curve, local and average heat transfer coefficients, and pressure drop. The second part will be dedicated entirely to CHF measurement and modeling. Key findings from this part are as follows:

(1) For horizontal flow, the effects of gravity are reflected in appreciable stratification across the channel. For the bottom heated wall, gravity aids vapor removal from, and liquid return to the bottom wall. On the other hand, gravity leads to vapor accumulation along the top heated wall. For vertical upflow and vertical downflow, with both single-sided and double-sided heating, there is far better symmetry in vapor formation along the channel, with no apparent bias towards either wall.

(2) Gravity has a strong influence on the boiling curve for horizontal flow at low mass velocities, but differences in heat transfer performance between bottom wall and top wall heating decrease with increasing mass velocity. On the other hand, there are only minor differences in boiling performance between vertical upflow and vertical downflow.

(3) For all orientations, the local heat transfer coefficient shows an appreciable decline in the inlet region, followed by a rather flat variation in the middle region, and a large increase in the exit region. The decrease in the inlet region is attributed to thermal boundary layer development, while the downstream increase is most likely the result of appreciable flow acceleration towards the exit.

(4) For horizontal flows, large differences in peak heat transfer coefficient are observed between top wall and bottom wall heating for low mass velocities because of the aforementioned stratification phenomenon. On the other hand, peak heat transfer coefficient values are about equal for all orientations above $G \cong 800$ kg/m^2 s, proving inertia around this mass velocity is effective at negating any orientation effects. Overall, gravity effects are governed mostly by mass velocity and, to a far lesser extent, by inlet quality.

(5) Pressure drops at low mass velocities are fairly equal for vertical upflow and vertical downflow, but greater than for horizontal flows. However, equal pressure drop is achieved for all orientations above $G \cong 800$ kg/m^2 s for all inlet qualities excepting the case with single-sided heating and low quality of $x_{e,in} = 0.04–0.07$, for which the transition mass velocity is $G \cong 1200$ kg/m^2 s.

Acknowledgements

The authors are grateful for financial support of this project by the National Aeronautics and Space Administration (NASA) under Grant No. NNX13AB01G, and technical support of the NASA Glenn Research Center, Cleveland, Ohio. This work was also supported by NASA Space Technology Research Fellowship NNX15AP29H.

References

[1] I. Mudawar, Two-phase micro-channel heat sinks: theory, applications and limitations, J. Electron. Packag. – Trans. ASME 133 (2011) 041002.
[2] P.J. Marto, V.J. Lepere, Pool boiling heat transfer from enhanced surfaces to dielectric fluids, J. Heat Transfer – Trans. ASME 104 (1982) 292–299.
[3] I. Mudawar, T.M. Anderson, Optimization of extended surfaces for high flux chip cooling by pool boiling, J. Electron. Packag. – Trans. ASME 115 (1993) 89–100.
[4] J.A. Shmerler, I. Mudawar, Local evaporative heat transfer coefficient in turbulent free-falling liquid films, Int. J. Heat Mass Transfer 31 (1988) 731–742.
[5] T.H. Lyu, I. Mudawar, Statistical investigation of the relationship between interfacial waviness and sensible heat transfer to a falling liquid film, Int. J. Heat Mass Transfer 34 (1991) 1451–1464.
[6] K.E. Gungor, R.H.S. Winterton, General correlation for flow boiling in tubes and annuli, Int. J. Heat Mass Transfer 29 (1986) 351–358.
[7] H.J. Lee, S.Y. Lee, Heat transfer correlation for boiling flows in small rectangular horizontal channels with low aspect ratios, Int. J. Multiphase Flow 27 (2001) 2043–2062.
[8] S. Mukherjee, I. Mudawar, Smart pumpless loop for micro-channel electronic cooling using flat and enhanced surfaces, IEEE Trans.-CPMT: Compon. Packag. Technol. 26 (2003) 99–109.
[9] M. Monde, T. Inoue, Critical heat flux in saturated forced convective boiling on a heated disk with multiple impinging jets, J Heat Transfer – Trans. ASME 113 (1991) 722–727.
[10] M.E. Johns, I. Mudawar, An ultra-high power two-phase jet-impingement avionic clamshell module, J Electron. Packag. – Trans. ASME 118 (1996) 264–270.
[11] D.D. Hall, I. Mudawar, Experimental and numerical study of quenching complex-shaped metallic alloys with multiple, overlapping sprays, Int. J. Heat Mass Transfer 38 (1995) 1201–1216.
[12] L. Lin, R. Ponnappan, Heat transfer characteristics of spray cooling in a closed loop, Int. J. Heat Mass Transfer 46 (2003) 3737–3746.
[13] M. Visaria, I. Mudawar, Theoretical and experimental study of the effects of spray orientation on two-phase spray cooling and critical heat flux, Int. J. Heat Mass Transfer 51 (2008) 2398–2410.
[14] M.K. Sung, I. Mudawar, Experimental and numerical investigation of single-phase heat transfer using a hybrid jet-impingement/micro-channel cooling scheme, Int. J. Heat Mass Transfer 49 (2006) 682–694.
[15] F.P. Chiaramonte, J.A. Joshi, Workshop on critical issues in microgravity fluids, transport, and reaction processes in advanced human support technology – final report, NASA TM-2004-212940, 2004.
[16] The National Academies, Recapturing a Future for Space Exploration: Life and Physical Sciences Research for a New Era, National Academies Press, Washington, DC, 2011.
[17] L. Zhao, K.S. Rezkallah, Gas–liquid flow patterns at microgravity, Int. J. Multiphase Flow 19 (1993) 751–763.
[18] A.E. Dukler, J.A. Fabre, J.B. McQuillen, R. Vernon, Gas–liquid flow at microgravity conditions: flow patterns and their transitions, Int. J. Multiphase Flow 14 (1988) 389–400.
[19] C. Colin, J. Fabre, A.E. Dukler, Gas–liquid flow at microgravity conditions – I. Dispersed bubble and slug flow, Int. J. Multiphase Flow 17 (1991) 533–544.
[20] C. Colin, J. Fabre, A. Kamp, Turbulent bubble flow in pipe under gravity and microgravity conditions, J. Fluid Mech. 711 (2012) 469–515.
[21] M. Saito, N. Yamaoka, K. Miyazaki, M. Kinoshita, Y. Abe, Boiling two-phase flow under microgravity, Nucl. Eng. Des. 146 (1994) 451–461.
[22] H. Ohta, Experiments on microgravity boiling heat transfer by using transparent heaters, Nucl. Eng. Des. 175 (1997) 167–180.
[23] Y. Ma, J.N. Chung, An experimental study of critical heat flux (CHF) in microgravity forced-convection boiling, Int. J. Multiphase Flow 27 (2001) 1753–1767.

[24] H. Zhang, I. Mudawar, M.M. Hasan, Flow boiling CHF in microgravity, Int. J. Heat Mass Transfer 48 (2005) 3107–3118.
[25] C. Konishi, H. Lee, I. Mudawar, M.M. Hasan, H.K. Nahra, N.R. Hall, J.D. Wagner, R.L. May, J.R. Mackey, Flow boiling in microgravity: Part 1 – Interfacial behavior and experimental heat transfer results, Int. J. Heat Mass Transfer 81 (2015) 705–720.
[26] C. Konishi, H. Lee, I. Mudawar, M.M. Hasan, H.K. Nahra, N.R. Hall, J.D. Wagner, R.L. May, J.R. Mackey, Flow boiling in microgravity: Part 2 – Critical heat flux interfacial behavior, experimental data, and model, Int. J. Heat Mass Transfer 81 (2015) 721–736.
[27] L.C. Chow, R.C. Parish, Condensation heat transfer in a microgravity environment, J. Thermophys. Heat Transfer 2 (1988) 82–84.
[28] A. Faghri, L.C. Chow, Annular condensation heat transfer in a microgravity environment, Int. Commun. Heat Mass Transfer 18 (1991) 715–729.
[29] L. Yuke, W. Weicheng, Condensation heat transfer inside a tube in a microgravity environment, J. Therm. Sci. 5 (1996) 184–189.
[30] E.D. Riva, D.D. Col, Effect of gravity during condensation of R134a in a circular minichannel, Microgravity Sci. Technol. 23 (2011) 87–97.
[31] H. Lee, I. Mudawar, M.M. Hasan, Experimental and theoretical investigation of annular flow condensation in microgravity, Int. J. Heat Mass Transfer 61 (2013) 293–309.
[32] H. Zhang, I. Mudawar, M.M. Hasan, Experimental assessment of the effects of body force, surface tension force, and inertia on flow boiling CHF, Int. J. Heat Mass Transfer 45 (2002) 4079–4095.
[33] H. Zhang, I. Mudawar, M.M. Hasan, Experimental and theoretical study of orientation on flow boiling CHF, Int. J. Heat Mass Transfer 45 (2002) 4463–4477.
[34] C. Konishi, I. Mudawar, Investigation of the influence of orientation on critical heat flux for flow boiling with two-phase inlet, Int. J. Heat Mass Transfer 61 (2013) 176–190.
[35] C.R. Kharangate, I. Mudawar, M.M. Hasan, Photographic study and modeling of critical heat flux in horizontal flow boiling with inlet vapor void, Int. J. Heat Mass Transfer 55 (2012) 4154–4168.
[36] C.R. Kharangate, I. Mudawar, M.M. Hasan, Experimental and theoretical study of critical heat flux in vertical upflow with inlet vapor void, Int. J. Heat Mass Transfer 55 (2012) 360–374.
[37] C.R. Kharangate, L. O'Neill, I. Mudawar, M.M. Hasan, H.K. Nahra, R. Balasubramaniam, N.R. Hall, A.M. Macner, J.R. Mackey, Flow boiling and critical heat flux in horizontal channel with one-sided and double-sided heating, Int. J. Heat Mass Transfer 90 (2015) 323–338.
[38] C.R. Kharangate, L. O'Neill, I. Mudawar, M.M. Hasan, H.K. Nahra, R. Balasubramaniam, N.R. Hall, A.M. Macner, J.R. Mackey, Effects of subcooling and two-phase inlet on flow boiling heat transfer and critical heat flux in a horizontal channel with one-sided and double-sided heating, Int. J. Heat Mass Transfer 91 (2015) 1187–1205.
[39] C.R. Kharangate, L. O'Neill, I. Mudawar, Effects of two-phase inlet quality, mass velocity, flow orientation, and heating perimeter on flow boiling in a rectangular channel: Part 2 – CHF experimental results and model, Int. J. Heat Mass Transfer 103 (2016) 1280–1296.
[40] W. Li, Z. Wu, A general criterion for evaporative heat transfer in micro/mini-channels, Int. J. Heat Mass Transfer 1967–1976 (2010).
[41] Z. Wu, W. Li, S. Ye, Correlations for saturated critical heat flux in microchannels, Int. J. Heat Mass Transfer 54 (2011) 379–389.
[42] W. Li, Z. Wu, Generalized adiabatic pressure drop correlations in evaporative micro/mini-channels, Exp. Therm. Fluid Sci. 35 (2011) 866–872.